Is the Cu/Zn Disorder the Main Culprit for the Voltage Deficit in Kesterite Solar Cells?

Stéphane Bourdais, Christophe Choné, Bruno Delatouche, Alain Jacob, Gerardo Larramona, Camille Moisan, Alain Lafond, Fabrice Donatini, Germain Rey, Susanne Siebentritt, Aron Walsh, and Gilles Dennler**

Photovoltaic thin film solar cells based on kesterite $Cu_2ZnSn(S_x,Se_{1-x})_4$ compounds (CZTSSe) have reached >12% sunlight-to-electricity conversion efficiency. This is still far from the >20% record devices known in $Cu(In_{1-y},Ga_y)Se_2$ and CdTe parent technologies. A selection of >9% CZTSSe devices reported in the literature is examined to review the progress achieved over the past few years. These devices suffer from a low open-circuit voltage (V_{oc}) never better than 60% of the $V_{oc\ max}$, which is expected from the Shockley-Queisser radiative limit (S-Q limit). The possible role of anionic (S/Se) distribution and of cationic (Cu/Zn) disorder on the V_{oc} deficit and on the ultimate photovoltaic performance of kesterite devices, are clarified here. While the S/Se anionic distribution is expected to be homogeneous for any ratio x, some grain-to-grain and other non-uniformity over larger area can be found, as quantified on our CZTSSe films. Nevertheless, these anionic distributions can be considered to have a negligible impact on the V_{oc} deficit. On the Cu/Zn order side, even though significant bandgap changes (>10%) can be observed, a similar conclusion is brought from experimental devices and from calculations, still within the radiative S-Q limit. The implications and future ways for improvement are discussed.

1. Introduction

During the last decade, photovoltaic devices based on copper zinc tin sulfo-selenide $Cu_2ZnSn(S_xSe_{1-x})_4$ (CZTSSe) thin films have experienced a significant increase in efficiency,[1] evolving from about 5% in 2004 up to 12.6% in 2013.[2] However, a kind of saturation has seemed to occur recently: As of today (end of 2015), the highest efficiency publicly released is still the 12.7% reported jointly by the IBM and Solar Frontier teams in 2014.[3] In other words, no major progress has occurred during the last two years as far as the record efficiency of CZTSSe devices is concerned. Looking carefully at the historical evolution of the best research-cell efficiency on the now famous chart regularly updated by the US National Renewable Energy Laboratory (NREL),[4] one would note that such a temporary stagnation is not rare, especially during the four decade long development of the $Cu(In_{1-y},Ga_y)Se_2$ (CIGSe) and CdTe parent thin-film technologies. Inevitably, these periods are prone to legitimate questioning about the ultimate potential of a given material under scrutiny.

Various reasons have been proposed in the literature to explain the current difference in efficiency observed between CZTSSe and CIGSe devices, considering that their respective optical bandgaps E_g are very close. All converge toward the low open-circuit voltage (V_{oc}), or large V_{oc} deficit ($V_{oc\text{-}def}$), observed unanimously, which is defined as:

$$\Delta V = V_{oc\text{-}def} = \frac{E_g}{q} - V_{oc} \quad (1)$$

Dr. S. Bourdais, C. Choné, B. Delatouche, Dr. A. Jacob, Dr. G. Larramona, C. Moisan, Dr. G. Dennler
IMRA Europe S.A.S
220, rue Albert Caquot, BP 213
06904 Sophia Antipolis, France
E-mail: bourdais@imra-europe.com; dennler@imra-europe.com

Prof. Dr. A. Lafond
Institut des Matériaux Jean Rouxel (IMN)
Université de Nantes
CNRS 2, rue de la Houssinière BP 32229
44322 Nantes Cédex 03, France

Dr. F. Donatini
Université Grenoble Alpes
Institut NÉEL
F-38042 Grenoble, France

Dr. F. Donatini
CNRS
Institut NÉEL
F-38042 Grenoble, France

Dr. G. Rey, Prof. Dr. S. Siebentritt
Laboratory for Photovoltaics
Physics and Materials Science Research Unit
University of Luxembourg
41, rue du Brill, L-4422 Belvaux, Luxembourg

Prof. Dr. A. Walsh
Center for Sustainable Chemical Technologies
Department of Chemistry
University of Bath
Bath, UK

Prof. Dr. A. Walsh
Global E3 Institute and Department of Materials Science and Engineering
Yonsei University
Seoul 120–749, Korea

DOI: 10.1002/aenm.201502276

© 2016 WILEY-VCH Verlag GmbH & Co. KGaA, Weinheim

where q is the elemental charge. It has been proposed, and seemingly quite accepted, that the natural bulk properties of the CZTSSe crystal may explain a large part of this V_{oc} deficit.[5] More precisely, strong band tailing originating from large densities of variably compensated point defects have been invoked.[6]

As a matter of fact, the Cu and Zn atoms comprised in the kesterite structure of CZTSSe can swap at fairly low enthalpic cost, thereby inducing the so called "Cu/Zn disorder" in the kesterite structure.[7] Note that this issue does not exist in the chalcopyrite crystalline structure of CIGSe due to the larger chemical mismatch between Cu and In/Ga. Surprisingly, the potential implications of this structural instability upon the charge carrier transport and performance of CZTSSe photovoltaic devices have been somewhat neglected until a reversible transition with temperature was evidenced in 2014.[8] Since then, a few groups have reported similar results on this order/disorder (O/D) transition which has been found to occur at quite low temperatures (≈200 °C, see Section 4).[8–10] However, to the best of our knowledge, no clear experimental correlations have been made yet between this O/D transition, the V_{oc} deficit in kesterite devices, and the alleged limitations of CZTSSe regarding its overall photovoltaic potential. It remains an open question whether or not the O/D, which is known to cause reversible bandgap changes,[9] is the culprit for the experimental observations of the V_{oc} deficit and of the above-mentioned band tailing. This report addresses this question by critically reviewing and underlining some recent progresses, adding some pertinent new experimental observations and theoretical understanding, towards the next major breakthroughs in the field of kesterite solar cells.

In the first part of this article, we review the best CZTSSe devices published in the literature (efficiencies higher than 9%) and underline the most effective technological findings that have recently been proven to increase their performances. In the second part, we focus on the main loss mechanisms reported to hinder the performances of kesterite solar cells, especially compared to their CIGSe counterpart. The third part aims at summarizing the present knowledge of the O/D transition and its impact on CZTSSe properties, mostly structural and optical. Finally, the fourth part is dedicated to an in depth discussion, fueled by new data, answering partially some questions, yet raising some others. We then conclude all the major observations, and suggest the way forward to: i) better assess the overall photovoltaic potential of CZTSSe, and ii) increase the efficiency of the CZTSSe solar cells in the short term.

2. Review of Some Major Recent Progresses in CZTSSe Devices

Typical efficient CZTSSe solar cells consist of a vertical stack of several layers having the general form glass/Mo/Mo$(S_ySe_{1-y})_2$/$Cu_2ZnSn(S_xSe_{1-x})_4$/CdS/i-ZnO/TCO/Ni/Al, where the transparent conducting oxide (TCO) is Sn-doped indium oxide (ITO) or Al-doped zinc oxide (AZO); optionally a MgF_2 anti-reflection coating (ARC) is added on top of the Ni/Al metal grid, especially in record devices. In most of the cases, the CZTSSe absorber layer is prepared by a two-step approach comprising: i) a deposition of an intermediate thin film, followed by ii) a

Stéphane Bourdais holds an engineering degree from the National Institute of Applied Science (INSA Rennes, France) and a Ph.D. in Semiconductor Physics received in 2000 from the University of Strasbourg, France. After a first career on developing prototype thin film deposition equipments at semiconductor industry manufacturers Jipelec S.A.S., Alcatel MMS S.A. and Unaxis S.A.S., he joined IMRA Europe in 2007 as Project Leader of photovoltaic research programs. He initiated the activity on CZTS spray deposition from aqueous colloidal solutions. His current scientific interests focus on innovative inorganic semiconductor materials for life, energy and environment applications.

Gerardo Larramona studied Chemistry at the University of Barcelona (Spain) and obtained his Ph.D. in Chemistry at the Autonomous University of Madrid (Spain) in 1989. He worked a few years as researcher at the University of Southampton (UK) and at the Spanish National Research Council (CSIC) in Madrid in the field of spectro-electrochemistry. In 1992, he moved to IMRA Europe (France), where he now serves as Project Leader. His scientific expertise covers several topics like metal hydrides, microelectrodes, electrochemical Peltier devices, gas sensors, fuel cells, and photovoltaic cells.

Gilles Dennler obtained a Ph.D. in Plasma Physics at the University of Toulouse (France) and a Ph.D. in Experimental Physics at Ecole Polytechnique of Montréal (Canada). In 2003, he moved to the Linz Institute for Organic Solar Cells (Austria) directed by Prof. N. S. Sariciftci, where he was appointed Assistant Professor. In 2006, he joined Konarka Technolgies Inc. (Linz, Austria and then Lowell MA, USA) where he served as Director of Research. In 2011, he took the lead of the Energy and Environment Department at IMRA Europe (France). His research interests span from organic electronics to inorganic solar cells and innovative thermoelectric materials.

© 2016 WILEY-VCH Verlag GmbH & Co. KGaA, Weinheim

Table 1. Selection of CZTSSe solar cells with efficiency above 9%.

	Affiliation	Material [E_g, eV]	Method	T [°C]	η [%]	J_{sc} [mA cm^{-2}]	V_{oc} [mV]	FF [%]	Area [cm^2]	Year	Ref.
Non-Vacuum	**IBM/Solar Frontier**	CZTSSe (1.07)	Spin-on+ dual buffer	>500	12.7	38.9	466	69.8	0.45	2014	[3]
	IBM	CZTSSe (1.13)	Spin-on (x3+)+N_2	>500	12.6 c	35.2	513	69.8	0.42	2013	[2]
	University of Washington	CZTSSe (1.04)	Spray+Se	540	11.8	38.8	449	68.1	0.10	2015	[13]
	EMPA	CZTSSe (1.05)	Spin-on (x14)+Se	550	11.2	36.5	479	63.8	0.30	2015	[14]
	IMRA Europe	CZTSSe (1.17)	Spray+Se+ dual buffer	570	10.9	32.2	520	65.0	0.25	2015	[15]
	ZSW	CZTSSe	Spin-on (x6)+$SnSe_2$	540	10.3 c	31.6	471	69.6	0.25	2015	[16]
	Purdue University	CZTGSSe (1.18)	Doctor blade+Se	500	9.4	31.9	460	63.8	0.47	2015	[17]
	Nanyang Technol. Uni.	CZCTS (1.38)	Spin-on (x10)+S	580	*9.2	24.1	581	66	0.25	2015	[18]
	Dupont De Nemours	CZTSSe (1.07)	Doctor blade+Se	550	9.02	32	445	63.3	–	2015	[19]
	Purdue University	CZTSSe (1.13)	Doctor blade+Se	500	9.0	35.1	404	63.7	0.48	2015	[20]
Vacuum	**Solar Frontier**	CZTSSe	Sputttering+S+Se	–	11.8	35.1	503	66.8	14	2015	[21]
	IBM	CZTSe (1.0)	Co-evaporation+Se	590	11.6	40.6	423	67.3	0.43	2014	[22]
	Solar Frontier and TIT	CZTSSe	Sputttering+S+H_2Se?	–	*10.5	38.2	429	63.8	–	2015	[23]
	IREC	CZTSe (1.04)	Sputtering+Ge+Se	550	*10.1	33.3	453	66.8	0.09	2015	[24]
	NREL	CZTSe (0.97)	Co-evaporation	500	9.8 c	37.5	380	68.9	0.42	2014	[25]
	IMEC	CZTSe (0.97)	Sputtering+H_2Se	500	9.7	38.9	408	61.4	1	2013	[26]
	Toyota Central Labs	CZTS (1.47)	Sputtering+H_2S	580	9.1 c	20.6	0.70	62.5	0.24 da	2013	[27]
	Solar Frontier	CZTS (1.47 ?)	Sputttering+H_2S?	–	9.2	21.6	708	60.1	14	2013	[28]

*without MgF_2 anti-reflection coating; da: designated illumination area; c: certified.

high temperature (T > 500 °C) annealing in various gaseous environments.

An overview of the most efficient kesterite solar cells reported to date in the literature is shown on **Table 1**. It covers a large composition range going from pure selenide $Cu_2ZnSnSe_4$ (CZTSe, $E_g \approx 1.0$ eV) to pure sulfide Cu_2ZnSnS_4 (CZTS, with $E_g \approx 1.5$ eV). We have purposely separated the vacuum-based and liquid-based processes, as they appear as two competing routes having their respective specificities. The current record is still the 12.7%[3] fabricated from a hydrazine solution and including: i) an optimization of the light management within the whole devices,[11] ii) an effective grain boundary passivation,[12] and iii) the use of an In_2S_3/CdS dual buffer layer.[3] All these major enhancements, plus some others, are discussed below.

2.1. Light Management

Although light management is largely studied in various other types of solar cells,[29] the optics in kesterite devices was not optimized until recently. In 2014, Winkler et al. performed a complete light management study that combined optical modeling of idealized planar devices with a semi-empirical approach accounting for the surface roughness of the various layers.[11] This allowed them to: i) strongly decrease the parasitic absorption in the CdS layer by reducing its thickness from 50 to 23 nm, and simultaneously ii) maximize the constructive interferences (and minimize the destructive interferences) within the CZTSSe photoactive film by reducing the thickness of the TCO+i-ZnO layers from 240 nm down to 55 nm. It is worth noting that Winkler et al. had to redesign appropriately the Ni/Al grid in order to account for the higher sheet resistance of the thinner TCO window layer, without increasing the shadowing loss above 5%. A similar optical study has been conducted by ElAnzeery et al., yet in pure selenide CZTSe devices.[30] In this latter work, the thicknesses of the various layers within the optimized CdS/i-ZnO+AZO/MgF_2 stack were 20/435/130 nm, respectively, what yielded a short circuit current density (J_{sc}) close to 40 mA cm^{-2}. The deposition of the "as thin as possible" CdS buffer layer (around 20 nm) without a shunting issue, was achieved by a so-called "cadmium treatment",[31] which also happened to decrease the series resistance of the device, thereby improving the Filling Factor (FF) and the overall photovoltaic performance.

2.2. Grain Boundaries Passivation

Alike in any polycrystalline materials used in photovoltaic devices,[32] grain boundaries in CZTSSe are the usual suspects when it comes to the swift, non-radiative recombination of charge carriers. It has been shown recently by Sardashti et al. that grain boundaries in CZTSSe can be efficiently passivated by growing a thin (100–300 nm) layer of SnO_x around the grains.[12] This critical process step was performed prior to the deposition of the CdS film, by i) annealing the active layer in air (375 °C for 2 min) in order to oxidize the metal rich interfaces, and ii) applying a NH_4OH-based wet etch (5 min dip in 7% aqueous NH_4OH solution) to remove the newly created metal oxides (except SnO_x). In a similar way, a 30 min air annealing at

© 2016 WILEY-VCH Verlag GmbH & Co. KGaA, Weinheim

150 °C, followed by a wet aqueous chemical cleaning (thiourea and/or HCl dip), was found necessary for Furuta et al.[23] to reach >10.5% efficient devices (without ARC). This intentional oxidation appears quite similar to the one previously advocated by Repins et al. which allowed them to achieve 9.15% with co-evaporated CZTSe absorbers fabricated with a very Zn-rich terminated surface.[33]

Some previous reports claimed that exposure to air after the high temperature selenization step and prior to the buffer deposition has to be avoided as much as possible.[34–36] We would like to underline at this point that all these air annealing steps are performed at relatively low temperatures (150–375 °C), yet high enough to potentially modify the O/D nature of the kesterite crystals. This will be further discussed in Section 3 of this report.

2.3. Dual Buffer Layer

The vast majority of the efficient CZTSSe devices published in the literature employ a CdS buffer layer. However, it has been recently shown that a CdS/In_2S_3 dual buffer (or hybrid buffer), in which a thin In_2S_3 is deposited atop the CdS film, can enable a reproducible and noticeable increase of about 70 mV in the V_{oc} of pure sulfide[37] and sulfo-selenide kesterite devices.[2] It has been proposed by Kim et al.[3] that the improvement in the V_{oc} stems from an enhanced free hole carrier density induced by the diffusion of p-doping In within the CZTSSe active layer.

2.4. Hydrazine-Free Liquid Processes

The process leading to the most efficient kesterite solar cells is still the one based upon hydrazine (NH_2-NH_2) solutions.[2] However, the high toxicity of hydrazine (by simple contact or inhalation), its very low auto-ignition temperature (24 °C on iron rust surface) and flash point (38 °C in ambient air) significantly jeopardizes the up-scaling and industrialization of this fabrication route. This major drawback has strongly motivated the search for alternative liquid processes employing less, or even non-hazardous solvents. Agrawal et al. were first to develop performing devices by coating colloidal inks based on well-crystallized CZTS nanoparticles of about 20 nm in diameter dispersed in hexanethiol.[20,38] Wu et al. developed a somewhat similar process, yet based upon binary and ternary metal chalcogenide nanoparticles coated from a tetrahydrofuran (THF) ink.[19,39] Both approaches allowed to reach efficiencies of 9% or more, even if in the latter case a fine grained, carbon-rich film appeared at the bottom of the CZTSSe layer.[19]

Another successful and largely deployed liquid approach consists of coating molecular inks formed by dissolving copper, zinc and tin precursors (mostly acetates or chlorides thereof) with thiourea in DMSO solvent and annealing them in an appropriate gaseous environment.[40] This route is very different from the former one in that the printed ink does not contain nanoparticles of metal sulfides, only the chemical precursors necessary to grow CZTS. As of today, several teams employing this approach have reached efficiencies higher than 10%.[13,14,16] Here again, carbon residues from the solvent have been reported to remain in some instances, and appeared at the bottom of the CZTSSe absorber layer. Interestingly and contrarily to other semi-conductors, CZTSSe appears quite tolerant to carbon impurities. Indeed, ab initio calculations have indicated the absence of carbon related point defects with ionization energy levels within the bandgap of the photo absorber.[41] Some countermeasures were proposed recently to significantly improve the morphology of such carbon-containing films: For example, annealing under $SnSe_2$ rich (instead of Se rich) conditions achieved large-grained-CZTSe single layers from DMSO-based ink, which contributed in the recent 10.3% reported by Schnabel et al.[16] Along the same lines, Haass et al. enhanced their precursor solution process by employing a three stage annealing sequence, leading them to efficiencies as high as 11.2%.[14]

It is worth noting that a third effective alternative liquid process was reported recently by Larramona et al.[42] This approach appears as an intermediate situation between the now standard colloidal dispersion mentioned above (containing well crystallized, size controlled nanoparticles) and the fully liquid, molecular ink. The procedure relies on an ink containing partially amorphous CZTS nanoparticles formed at room temperature by instantaneous precipitation reaction (to be compared with the several hour long synthesis necessary to generate the well crystallized, size-controlled nanoparticles).[42,43] Furthermore, this process enjoys a major competitive advantage, paving the way to its potential industrialization, in that the ink used to spray coat the active layer is made of 90% water and 10% ethanol. Efficiencies close to 11% were reported recently for devices fabricated this way.[15]

From Table 1, the best device efficiencies achieved from hydrazine-free solution routes can be considered in par with vacuum-based devices; for instance, sequentially co-evaporated then selenized CZTSe films based devices by IBM included the above-mentioned optical stack optimization and have reached 11.6%.[22]

Finally, we have to mention the growing interest in the electrodeposition of kesterite solar cells[44,45] even though the best devices prepared by this approach are still slightly lower in efficiency[46] and have not yet passed the 9% threshold.

2.5. Additional Elements in the CZTSSe Active Layer

In order to enhance the photovoltaic performances of CZTSSe devices, many chemical elements have been added as traces, impurities, or sizable amounts. The most noticeable cases are listed below:

- Sodium, in concentrations of up to about 1% (atomic) has been found beneficial to enhance the size of the kesterite grains in pure CZTS,[47] pure CZTSe,[48] and sulfo-selenide CZTSSe.[15] Moreover, Na has been shown to influence significantly the number of charge carriers present in the photoactive layer in the dark.[49]
- Lithium impurity may act in a similar way as Na on kesterite grains properties, but was proposed to cause electric field inversion recently evidenced at grain-boundaries. A record 11.8% device was achieved by this approach, employing a molecular solution-based CZTSSe absorber.[13]

© 2016 WILEY-VCH Verlag GmbH & Co. KGaA, Weinheim

- Antimony, like Na, was reported to promote the crystallization of CZTSSe[50–52] by acting as a fluxing agent. It is even suspected to hinder the formation of the carbon-rich layer that appears in some solution processed kesterite layers.[50]
- Germanium, when used in a quantity large enough to create an alloy with CZTSSe (thereby forming $Cu_2Zn(Sn_{1-y}Ge_y)(S_x,Se_{1-x})_4$ with $0 \le y \le 1$) has been used to tailor the bandgap of the kesterite photoactive materials by a factor 2, from about 1.07 eV for CZTSe to 1.91 eV for CZGS.[53] Following this path, a 9.4 % device was reported based on a Ge amount of Ge/(Sn+Ge) = 30%.[17] Furthermore, by using traces of Ge, Giraldo et al. have recently been able to enhance the morphology of vacuum-deposited CZTSe-based devices, and to improve the performance from 7 to 10.1%.[24]
- Cadmium, like Na, Sb or Ge, is known to be an efficient fluxing agent. In parallel to grain size enlargement, a complete reduction of the ZnS secondary phase was achieved by alloying pure sulfide CZTS with Cd. The device efficiency increased from 5% to more than 9% at optimum $Cu_2(Zn_{0.6},Cd_{0.4})SnS_4$ composition. Furthermore, sharper absorption edges indicate a possible reduction in Cu-Zn disorder, due to Zn substitution with Cd.[18]
- Silver alloying was recently shown to enhance the morphology of $(Cu_{1-x}Ag_x)_2ZnSnSe_4$ layers. Continuous films with x up to 50% were characterized with a grain size 2 to 3 times larger than the thickness of the film while no secondary phases were detected.[54] Increasing the Ag content also resulted in improved charge carrier lifetime and sharper absorption edges, again indicative of a possible reduction of Cu/Zn disorder via elemental substitution of Cu with Ag.

2.6. Vertical Bandgap Gradient

One of the main breakthroughs that has allowed CIGSe devices to pass the 20% threshold[55] was the completion of an optimized vertical gradient of the photoactive bandgap. This was achieved by controlling carefully the In/Ga composition profile.[56] Naturally, the realization of the same kind of bandgap grading in kesterite devices is being pursued, although the main leverage investigated so far is the x = S/(S+Se) ratio profile. For instance, Kato et al. reported 11% efficiency CZTSSe devices achieved by having a back side enriched in sulfur and a front side enriched in Se.[57] Moreover, attempts to make a sulfur rich surface were tried in order to form a double graded bandgap.[58] However, this target appeared more difficult to achieve because of some intermixing between S and Se in the bulk of the materials, and some issues to incorporate sulfur at the surface without jeopardizing the integrity of the kesterite crystal.[21] Alternatively, a bandgap gradient could be achieved through an inhomogeneous vertical concentration of Ge in the $Cu_2Zn(Sn,Ge)S_4$ absorber.[59]

3. V_{oc} Deficit as the Main Loss Parameter

In general, the principle cause of V_{oc} deficit (difference between optical bandgap and V_{oc}) in photovoltaic devices is the recombination of photogenerated charge carriers in the bulk material and at surfaces. Usually the voltage deficit is dominated by one particular recombination process, for example, trap-assisted Shockley-Read-Hall recombination in CIGSe films.

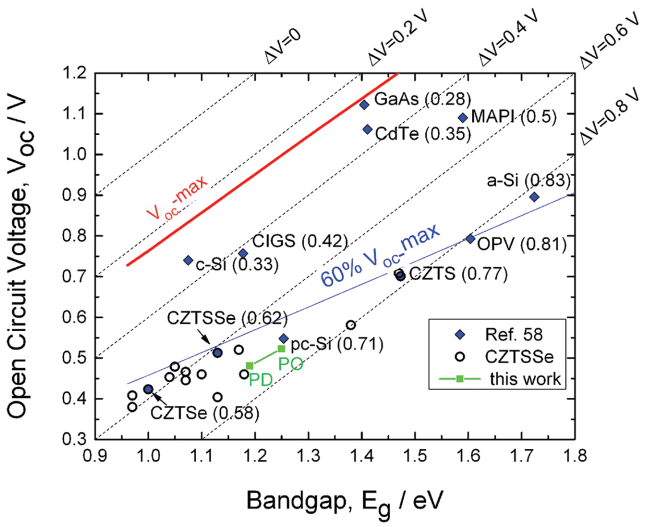

Figure 1. V_{oc} versus bandgap of CZTSSe devices from Table 1 (circles). Best devices based on other photovoltaic materials, as derived from [27] are added for comparison (diamond symbols): Methyl-ammonium lead iodide (MAPI), amorphous silicon (a-Si), organic photovoltaic films (OPV), crystalline silicon (c-Si) and polycrystalline silicon (pc-Si). The corresponding V_{oc} deficit values are mentioned in brackets. The oblique lines give a constant V_{oc} deficit from 0.8 V to 0 V. The green points correspond to our partially disordered (PD) and partially ordered (PO) CZTSSe films, as discussed in detail in Section 5.

Figure 1 shows V_{oc} versus the optical bandgap of all the CZTSSe devices listed in Table 1. The E_g values have been taken directly as reported in the respective publications. For the sake of comparison, we have added to the graph all the "best-in-class" single-junction solar cells for most of the current photovoltaic technologies, as listed in the latest version (V.46, Table I and III, July 2015) of the solar cell efficiency tables published biannually by Green et al.[27] Note that for all these latter devices, the optical bandgap has been estimated from the inflection point of the external quantum efficiency (EQE) curves, as proposed and detailed by Todorov et al.[60] As a guide to the eye, various oblique lines of fixed V_{oc} deficit values from $\Delta V = 0$ to 0.8 V were added, as well as the maximum achievable V_{oc} under 1-sun AM1.5G spectrum, using the calculation method detailed in [61].

Figure 1 illustrates unambiguously that kesterite solar cells generally suffer from a large V_{oc} deficit, and thereby have low V_{oc} values compared to the potential offered by their optical bandgap. As a matter of fact, all V_{oc} values of best CZTSSe devices are found below a line corresponding to 60% of the maximum achievable V_{oc}–max under one sun irradiation. The worst cases are observed for CZTS devices for which the V_{oc} deficit reaches values as high as 800 mV, comparable to the values measured for a-Si. Besides, the lowest V_{oc} deficits are achieved with CZTSSe kesterite having a small bandgap (1–1.2 eV) corresponding to low S/(S+Se) ratio. This confirms the trends already reported by Xie et al.[62] on vacuum processed devices and Gokmen et al.[6] on solution processed devices. As

© 2016 WILEY-VCH Verlag GmbH & Co. KGaA, Weinheim

a general observation, the lower the concentration of sulfur, the lower the V_{oc} deficit observed in CZTSSe devices, which appears correlated with the bulk properties of the absorber[63,64] and is even accentuated for devices using CdS buffer layers as discussed below.

3.1. Potential Interfacial Losses

As mentioned above, the V_{oc} deficit usually stems from either bulk or surface charge carrier transport limitation. Similar to the parent CIGSe technology, virtually all CZTSSe devices are based upon p-doped photoactive absorbers combined with the ubiquitous n-type CdS buffer. This p-n heterojunction evolves from a favorable spike-like interface at the conduction band edge in the case of pure CZTSe absorbers, to unfavorable cliff-like interface for CZTS absorbers, as discussed elsewhere[7] and further supported by recent simulations of pure-sulfide best devices.[65] Therefore some of the V_{oc} deficit observed in S-rich CZTSSe devices can be explained by a cliff-like conduction band offset (CBO) interface. In the Se-rich cases, the CBO at CdS/CZTSSe is not reported to significantly contribute to the V_{oc} deficit.

Regarding the back CZTSSe/Mo interface, the situation does not appear very problematic as far as V_{oc} deficit is concerned. As underlined by Polizzoti et al., the level of series resistance achieved in the best kesterite devices matches the state-of-the-art CIGSe solar cells, that is about 0.5 Ω cm^2.[5] Some concerns have been raised regarding the strong drop of *FF* and J_{sc} when the temperature of the solar cells is brought below 200 K, which has been tentatively attributed (among other hypothesis, see Section 3.2) to a potential barrier for carrier extraction located at the back contact of the photoactive layer.[66] However, it has not been proven yet that this potential barrier has any negative impact upon the performances of kesterite solar cells operating at room temperature (or above).[5]

3.2. Bulk Defects

3.2.1. Bulk Point Defects and Clusters

Similar to other inorganic crystals, kesterite is prone to point defects of all kinds, namely vacancies, antisites, and interstitials. Their formation is driven thermodynamically by minimizing the Gibbs free energy of the crystal. The fact that the material is comprised of 4 elements dramatically increases the number of possible defect types and complicates their characterizations. The enthalpy of formation of the most probable defects can be estimated by density functional theory (DFT), depending on the atomic chemical potentials of the cations present in the crystals. The top of **Figure 2** shows these enthalpies for 7 different chemical potentials (noted A to G) assuming that the Fermi level is at the top of the valence band.[67] One can see, for example, that the most likely point defect is the p-doping Cu_{Zn} antisite, whatever the growth conditions of the material. The calculations provide insights into the ionization potential of the various donor and acceptor defects, as illustrated in the bottom of Figure 2. The approximations involved in the computational procedure introduce a variability of +/– 50 meV in the defect levels. As pointed out by Han et al.[68] even though the concentration of Cu_{Zn} in CZTS is much higher than that of V_{Cu} the majority of the hole carriers could still be contributed by V_{Cu} because of the shallower level of V_{Cu} (50 meV) compared with that of Cu_{Zn} (110 meV) in pure Se cases. Thus, experimental defect analysis, as probed by admittance spectroscopy, often cite Cu_{Zn} as a likely source for free carriers, but others report V_{Cu} as the dominant acceptor defects (e.g., in the pure Se devices of Choudhury et al.[69]).

The same computational study by Chen et al. highlighted the likely presence of neutral defect clusters, made of compensating charged point defects. Such complexes may actually be more abundant than isolated defects due to the strong binding energy of the charged defects composing the cluster. The top of Figure 2 illustrates eloquently this effect: The cluster (Cu_{Zn} + Zn_{Cu}) turns out to be the most likely defect, independent of the atomic chemical potentials (except around the M point).

Another classification of point defect clusters has been proposed by Lafond et al.[71] and further developed by Gurieva et al.[72] This approach is considering off-stoichiometric compositions that result from charge-neutral substitution processes within the crystal grains, such as one Zn replacing two Cu ions, which writes $2Cu \rightarrow Zn_{Cu}+V_{Cu}$ (A-Type defect), or three added Zn in the place of two Cu sites and of one Sn site, $2Cu+Sn \rightarrow 2Zn_{Cu}+Zn_{Sn}$ (B-type defect). Six different defect clusters have been labeled this way so far (**Figure 3**). By comparing the top of Figure 2 and Figure 3, this simple approach captures the very same clusters as the ab initio methods, excluding the very probable defect cluster ($Cu_{Zn}+Zn_{Cu}$), which is present in virtually all points of Figure 3.

Most of the efficient devices reported in the literature operate in the "Cu-poor / Zn rich" region[70,74] in the middle, right-hand side of Figure 3. It has been thus concluded that A-type and B-type defects are not too detrimental to the device performances, while all of the others may be.[67]

3.2.2. Proven Effect of Bulk Defects upon CZTSSe Device Performances

As mentioned in the introduction, a direct comparison between kesterite and chalcopyrite solar cells should reveal important clues about the limitation of CZTSSe devices. Such an exercise was conducted by Mitzi et al., who studied simultaneously the transport properties of a 10.2% CZTSSe device and a 15.1% CIGSe device.[1] The two solar cells were produced with the same hydrazine process, and their respective photoactive layers had both an optical bandgap of 1.15 eV. Beyond the obvious differences related to their respective V_{oc} (517 versus 623 mV) and *FF* (64% versus 75%), Mitzi et al. observed a 100× increase of the series resistance in the CZTSSe device at temperature below 200 K, while the series resistance of CIGSe increased by only a factor of 3×. The observation was attributed to a so called "freeze-out effect" of the free carriers in CZTSSe at low temperatures, induced by the dominant presence of deep, partially compensated acceptor defects. Interestingly, this freeze-out has been effectively suppressed by adding indium traces in the

© 2016 WILEY-VCH Verlag GmbH & Co. KGaA, Weinheim

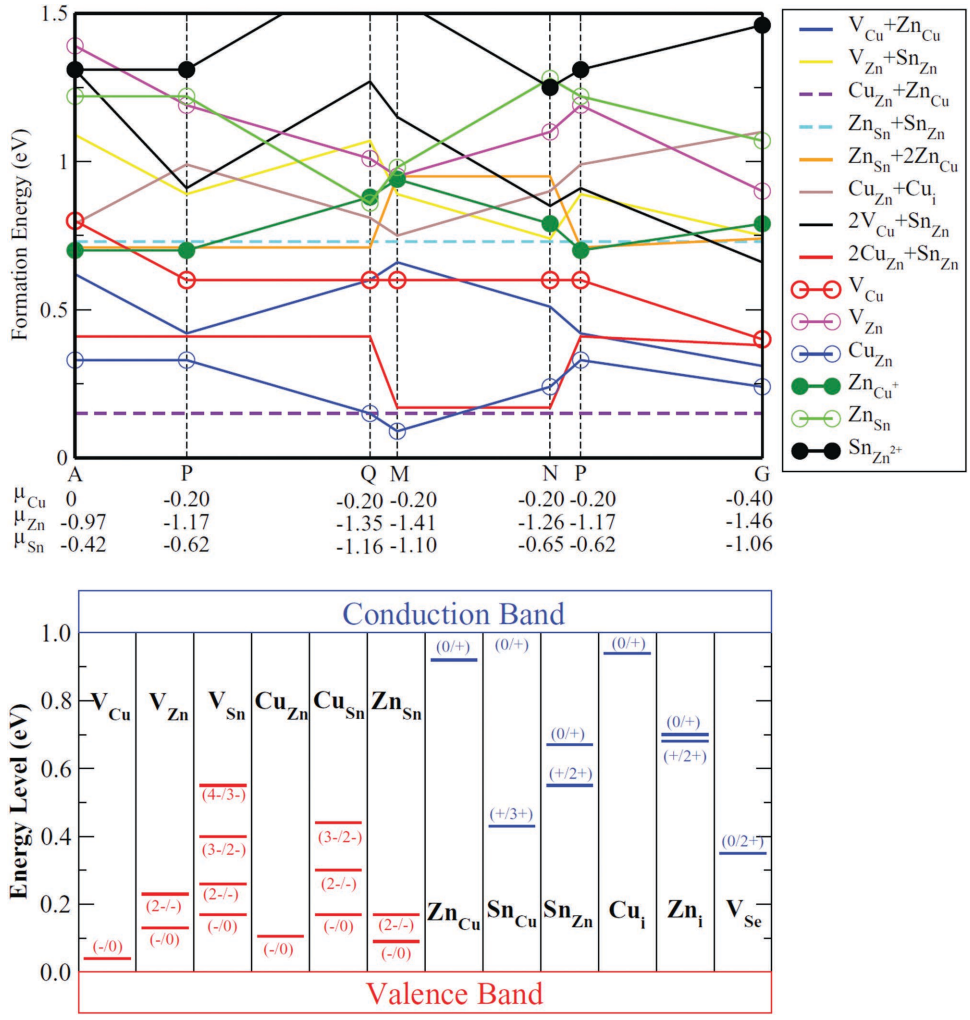

Figure 2. Upper panel: The formation energy of low-energy defects in $Cu_2ZnSnSe_4$ as a function of the chemical potential of the cations. The Fermi energy is assumed to be at the top of the valence band (strong p-type conditions), and all donor defects are fully ionized. Lower panel: The ionization levels of intrinsic defects in the bandgap of $Cu_2ZnSnSe_4$. The red bars show the acceptor levels and the blue bars show the donor levels, with the initial and final charge states labeled in parentheses. Reproduced with permission.[67] Copyright 2013, Wiley VCH.

active layer (thermal induced diffusion from an In_2S_3/CdS dual buffer) which supposedly acts as a shallow acceptor dopant.[2]

Further comparison between CZTS, CZTSSe and CIGSe films[63,78] carried out by photo-capacitance evidenced the presence of bulk, deep acceptor defects in S-rich kesterites. A defect, noted OH1, was located at 1 eV above the top of the valence band in pure sulfide CZTS (i.e., ≈0.5 eV below the conduction band), and found to be present at both low and room temperatures.[63] Even though detected at low temperatures in Se-rich CZT($S_{0.15}Se_{0.85}$) films (i.e., slightly below the conduction band), this OH1 defect was no longer detected at 300 K (by merging with the conduction band), which can also contribute to explaining the better photovoltaic performances achieved with Se-rich compounds.

Along the same lines, Larramona et al. have recently shown that fine tuning of the Sn content can be used to reduce both the number of deep traps (close to the middle of the band gap) and of the free carrier density within their CZTSSe active layer, resulting in a significant increase in device efficiencies, reaching values up to 10.8%.[15] A detailed transport study allowed them to attribute the presence of these detrimental deep defects to the lack of Sn within the kesterite structure. They tentatively incriminated V_{Sn} and/or Cu_{Sn} as the main culprit for the mid gap defects.

3.2.3. Band Tailing and its Potential Origin

Absorption tails located at the bandgap edges, generally characterized by Urbach energy (E_u), are known to act as non-radiative recombination paths and to affect the photovoltaic conversion efficiency.[76] Until today, E_u has never been reported from optical absorption measured on single crystal, self-supported samples, likely because CZTS compounds are generally fabricated as polycrystalline thin films on Mo/glass substrates. Therefore, alternative but more demanding methods have been used so far, such as quantum efficiency (QE) analysis, photoluminescence, or photocapacitance.[63,75] Photoluminescence measurements

© 2016 WILEY-VCH Verlag GmbH & Co. KGaA, Weinheim

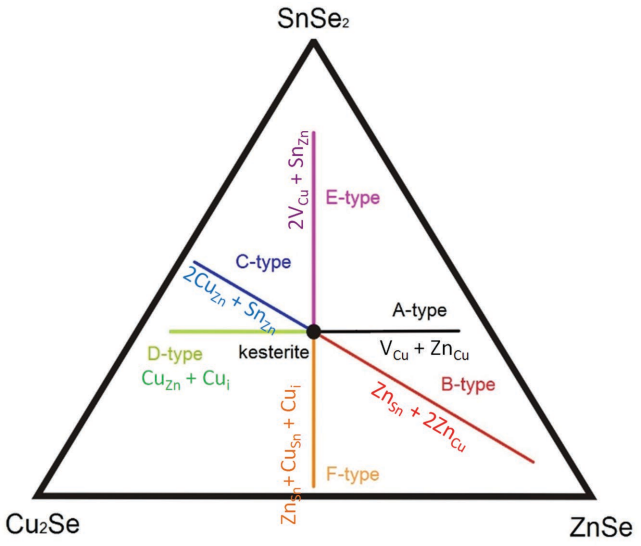

Figure 3. Classification of the clusters of point defects, and their existence versus the composition of the CZTSe layers, as described in the pseudo-ternary diagram of the three binary selenides.[72] Stoichiometric $Cu_2ZnSnSe_4$ is represented at the center of the triangle, corresponding to an equal mixture of Cu_2Se, ZnS and $SnSe_2$.

(PL) conducted on CZTSSe samples usually feature a much broader peak than those observed in standard CIGSe.[6,22,78] Moreover, the energy of the maximum of the PL peak (E_{PL}) of CZTSSe samples is usually noticeably red-shifted compared to their bandgap. These two features are generally attributed to band tailing, arising from either spatial bandgap variations or electrostatic potential fluctuations in the semiconductor (i.e., a constant bandgap with parallel shifts in the valence and conduction band energies).[6] Both effects lead to a non-zero density of states (DOS) within the band gap. The bandgap is either the energetic distance between the band edges, which is constant in the case of electrostatic potential fluctuations, or the average bandgap in the case of bandgap fluctuations (see **Figure 4**).

In both cases PL transitions are possible at peak energy E_{PL} lower than the (average) optical bandgap, E_g. In the case of bandgap fluctuations (Figure 4b), this red shift of the PL spectrum below E_g is caused by the presence of volumes with a lower bandgap and increases with the width of the bandgap distribution σ_g (standard deviation, assuming a Gaussian distribution), but is always larger than σ_g.[73] In the case of electrostatic potential fluctuations (Figure 4a), the PL emission energy is decreased because of non-local transitions. The energy shift is determined by Γ, the average potential fluctuation, which increases with increasing density of compensating donors and acceptors.[79] In many cases it is observed that such potential fluctuations disappear at room temperature, because of a sufficient density of free charge carriers, which screen the fluctuating potentials.[80] Thus with increasing disorder, either in terms of high densities of compensating defects (Γ) or in terms of different bandgaps (σ_g) the PL emission will shift further away from the (average) bandgap. This shift is caused by an increasing DOS within the band gap, reflected by an increasing Urbach energy. A red shift in the PL emission with respect to the bandgap will therefore reduce the maximal achievable open circuit voltage, even without interface recombination.[77,101] It has been observed that the red shift between E_{PL} and E_g at room temperature is particularly pronounced for pure sulfide CZTS (190 meV) and tends to reduce with increasing selenium content.[22,64] This appears consistent with an increase of the Urbach energy E_u observed with an increasing x = S/(S+Se) ratio.[63,75] This consideration suggests that some crystalline disorder present in the bulk of the absorber material, inducing bandgap fluctuations and band tailing, could explain a significant part of the V_{oc} deficit.

The red shift of the PL spectrum can be reduced by reducing the density of compensating (point) defects, but keeping a reasonable doping level, if the main cause is electrostatic potential fluctuations. However, as mentioned above electrostatic potential fluctuations are unlikely to play a significant role at room temperature. A further strategy to reduce the E_g–E_{PL} energy shift consists in reducing the bandgap fluctuations, which may arise either from i) non-uniform compositions at the microscopic level (typically below the sample thickness, i.e., <1 µm), ii) structural disorder in combination with i), or iii) from areas with different order state. For that matter, one needs to better understand its potential origin and means of control. This is discussed in the next section.

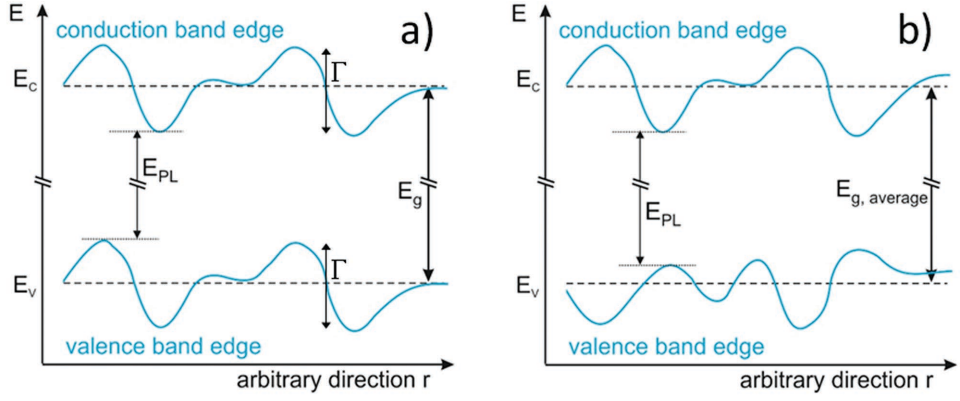

Figure 4. The effect of a) electrostatic potential fluctuations and of b) bandgap fluctuations. In each case radiative transitions at energies below the (average) bandgap are possible. Note that the bandgap in a) is constant and not affected by local charged defects, while band edges in b) can differ depending on e.g., long range composition variations.

© 2016 WILEY-VCH Verlag GmbH & Co. KGaA, Weinheim

4. Recent Reports on Order/Disorder

4.1. Cationic Disorder (Cu/Zn): Structural Changes

It is now generally accepted that CZTSSe crystals adopt a kesterite structure (*I*-4 space group), which is a tetragonal derivative of the cubic sphalerite ZnS structure.[82] The fully ordered kesterite lattice is shown in **Figure 5**. It is based upon an alternating sequence of two types of cationic planes along the c-axis, namely i) Cu and Sn containing planes located at z = 0 and z = 1/2 (*2a* Wyckoff sites occupied by Cu and *2b* sites occupied by Sn), and ii) Cu and Zn containing planes located at z = 1/4 and z = 3/4 (*2c* sites occupied by Cu and *2d* sites occupied by Zn).[83] Each of these cationic planes are separated by S/Se anionic planes (at z = 1/8, 3/8, 5/8, and 7/8). Ab initio calculations have shown at an early stage that the anti-site point defects Cu_{Zn} and Zn_{Cu} have very low enthalpies of formation, because of the similar charge (Δq = 1) and size of the two cations.[67] This result suggested that a disordered kesterite structure should exist at equilibrium, in which the *2c* and *2d* Wyckoff sites of the z = 0.25 plane are randomly occupied by the Cu^+ and Zn^{2+} cations. If this disorder is total, that is if *2c* and *2d* sites have the very same probability of being occupied by Cu or Zn, then a new symmetry is created: the fully disordered kesterite has the space group *I*-42*m*, in which the formerly *2c* and *2d* sites are all *4d* equivalent sites (Figure 5).

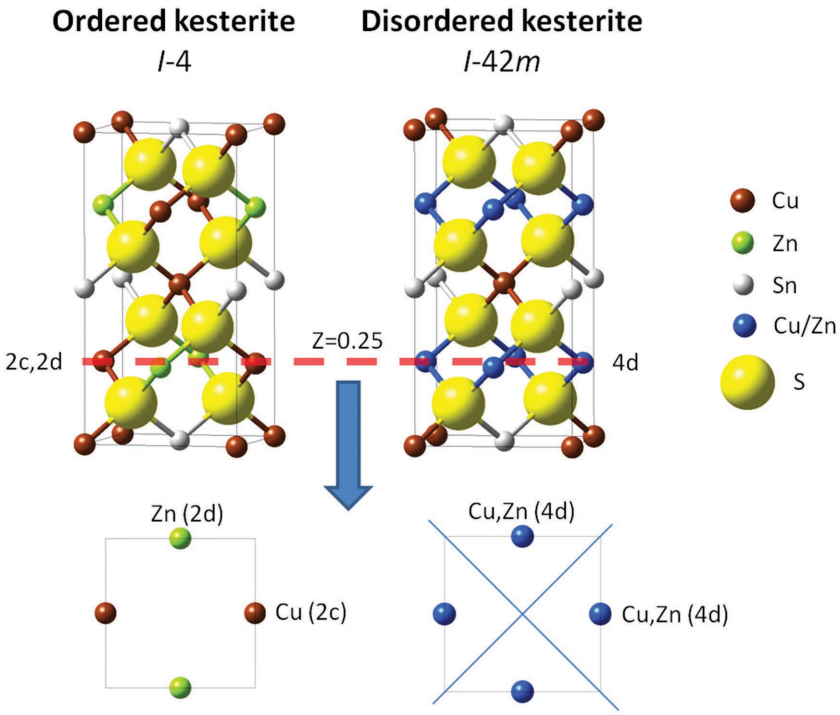

Figure 5. Representations of the ordered (*I*-4) and disordered (*I*-42*m*) CZTS kesterite crystalline structures. A projected view of the z = 0.25 plane is shown at the bottom. Adapted with permission.[71]

This theoretical prediction was actually preceded by experimental evidences of disordered kesterite, reported by Schorr et al. in 2007, and based upon neutron scattering measurements performed on $Cu_2Zn_xFe_{1-x}SnS_4$.[84] By applying a Rietveld analysis on the diffraction data, Schorr et al. showed that at x = 1 (CZTS), the *2a* and *2b* site were occupied by Cu and Sn exclusively, while Zn and the remaining Cu occupied the *2c* and *2d* positions in a disordered manner. The same conclusions could be drawn from resonant XRD diffraction[83] and from multinuclear (^{67}Zn, ^{119}Sn, ^{65}Cu) solid state nuclear magnetic resonance (NMR), which is a technique very sensitive to the cationic disorder in kesterite.[86]

In general, disordered kesterite samples are characterized by broader peaks width, as evidenced either from Raman (see **Figure 6**),[8] photoluminescence[87] or nuclear magnetic resonance[86] spectroscopy. In contrast, no peak broadening can be observed in XRD patterns measured in usual laboratory conditions (e.g., $Cu_{K\alpha}$, Bragg Brentano mode). Indeed, these are generally not sensitive enough to distinguish between the slight differences in the electronic environment of the (Ar)$3d^{10}$ configuration common to Cu^+ and Zn^{2+} ions.

Once the existence of the disordered kesterite was confirmed, leverages to control the level of O/D were investigated. From simple thermodynamic considerations, the entropy driven configurational disorder should increase with temperature.

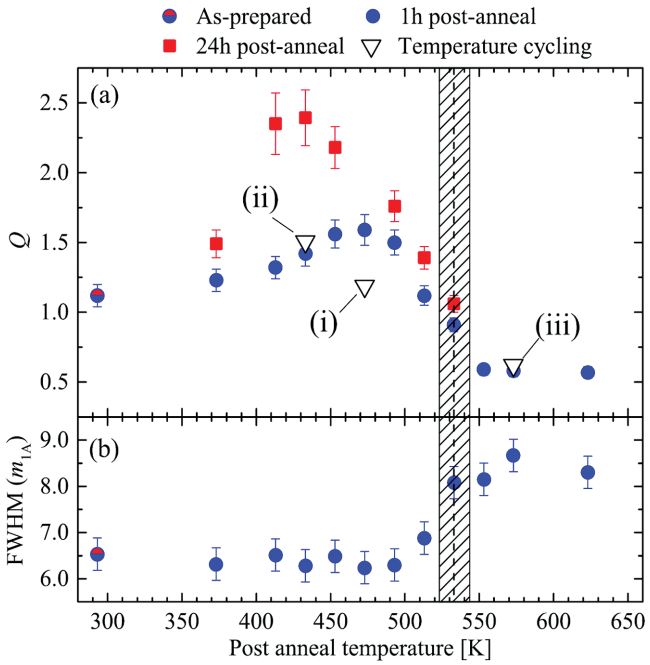

Figure 6. Variation in *Q* defined as $Q = I(m_{2A}) / I(m_{3A})$ for initially identical CZTS films post-annealed for different time periods. The triangles show the effect of temperature cycling on a single sample to test the reversibility of changes in *Q*. The shaded region indicates the probable location of the critical temperature T_C. Reproduced with permission.[8] Copyright 2014, AIP Publishing LLC.

© 2016 WILEY-VCH Verlag GmbH & Co. KGaA, Weinheim

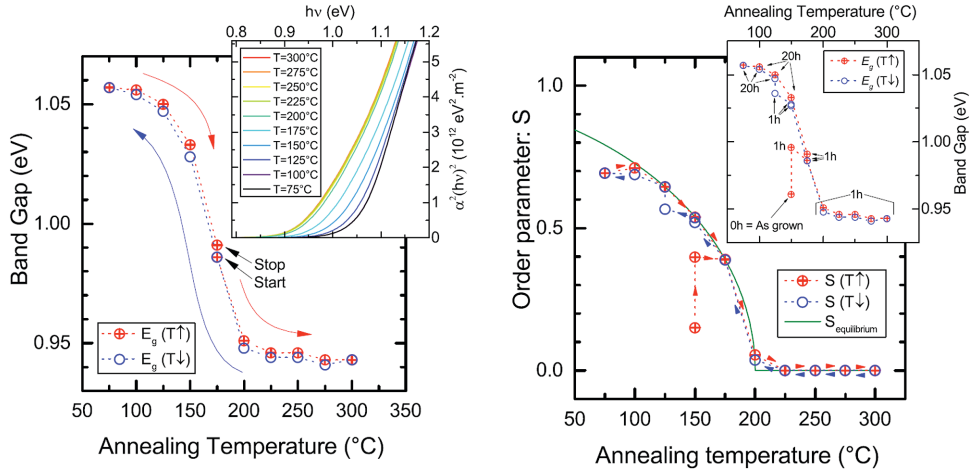

Figure 7. Left panel: Evolution of the CZTSe bandgap with temperature during the annealing/quenching sequence. Inset: Tauc plots for direct bandgap for decreasing temperature. Right panel: calculated evolution of the long-range order parameter during successive annealing. The inset presents the evolution of E_g for the same annealing sequence. Annealing times (dwell times) are shown as labels. Reproduced with permission.[9] Copyright 2014, AIP Publishing LLC.

Choubrac et al. showed using NMR that the cooling rate after synthesis has a tremendous effect on the O/D ratio in CZTS. More precisely, the slower the cooling, the more ordered the kesterite becomes.[86] For instance, dramatic disordering was found after cooling at rates faster than 10–24 K min^{-1}.[87] Further NMR and Raman studies confirmed the presence of A-type defect complexes (V_{Cu} + Zn_{Cu}), which tend to restrain the long-range Cu/Zn disorder.[90] Moreover, Raman investigations revealed that the transition from partially ordered to more disordered structure can be stimulated by optical excitation due to the small energy barrier between these two phases.[91]

The reversibility of the O/D transition was evidenced by Scragg et al. who studied the Raman spectra of CZTS samples having experienced various thermal treatments.[8] For that purpose, they defined the factor Q as the ratio of the m_{2A} (288 cm^{-1}) and m_{3A} (304 cm^{-1}) peak intensities, and attributed it to the Cu/Zn order. As illustrated in **Figure 6**, the larger Q, the more ordered the structure. They showed that above a critical temperature T_C, annealing followed by a swift cooling induced a large degree of disorder, while annealing below T_C helped to increase the amount of order. The critical temperature T_C was found to be about 533 K in this pure sulfide CZTS material. The transition was shown to be a thermodynamic order/disorder transition.

4.2. Optical Bandgap Changes

Building upon the observation of structural changes induced by thermal treatment, Rey et al. investigated the variation of the optical bandgap of CZTSe after successive annealing/quenching experiments: E_g was found to increase by 110 meV with decreasing annealing temperature.[9] In order to interpret their set of data, they applied Vineyard's theory of order-disorder kinetics and extracted a long-range order parameter, noted S.[85] Note that S = 1 corresponds to a perfectly ordered kesterite (which from theory is only accessible at zero absolute temperature, T = 0 K), $S = 0$ to a fully disordered kesterite, and $S = 0.875$ corresponds to a density of 3.4×10^{20} cm^{-3} (Zn_{Cu}+Cu_{Zn}) defect clusters. The right part of **Figure 7** shows that annealing the samples above the critical temperature for CZTSe (200 °C, 473 K) cancels entirely the order, and that the effect is reversible. Besides, the model proposed suggests that annealing at temperature as low as 75 °C still helps to enhance the order of the samples if it is undertaken for a long enough time.

Along the same lines, electro-reflectance[92] or quantum efficiency analysis[88] have been employed to observe the very same reversible E_g modification upon thermal treatment.

Surprisingly, no one has studied, on the same set of samples, both the structural O/D transitions and the optical bandgap changes. Even though the direct relationship proposed by Rey at al. between the optical bandgap and the Cu/Zn O/D seems plausible (if one refers to the correlations found in pure sulfide materials between Raman and NMR[90] or Raman and PL[89]) it has not been proven directly yet. Some additional clues can be found in theoretical studies however. For example, the bandgap of ordered kesterite CZTS has been reported to be 1.50 eV from hybrid density functional theory (HSE06 functional).[93] In the same study, the fully disordered kesterite (Figure 5-right) was considered with a 64 atom supercell generated using the special quasi-random structure approach. This results in a bandgap decrease of 40 meV (similar for the S and Se materials), consistent with but notably lower than experimentally observed. It should be noted that this model is designed more to assess thermodynamic quantities for a random alloy, and a better description of the disordered system would require sampling an ensemble of Cu/Zn distributions that can take into account spatial variations in the metal distributions over larger areas. Chen at al. concluded that when a 128 atom supercell contains one (Cu_{Zn}+Zn_{Cu}) cluster, the bandgap change induced in CZTS or CZTSe is negligible because of the hybridization between Cu_{Zn} acceptor and Zn_{Cu} donor states.[67] A more significant alteration of the bandgap is induced by defect clusters composed of deep level defects, such as Sn_{Zn}, Sn_{Cu}, Cu_{Sn} and Zn_i. Huang et al. calculated by the same method that one (Cu_{Zn}+Zn_{Cu}) cluster within a 32 atom CZTS supercell, which corresponds to an ordered defect structure (and not disordered), decreases the bandgap of the material by about 110 meV. On the other hand, the A-type cluster (V_{Cu}+Zn_{Cu}) was found to

© 2016 WILEY-VCH Verlag GmbH & Co. KGaA, Weinheim

increase E_g by 70 meV.[94] These somewhat contradictory results have been recently clarified by Scragg et al. who calculated 64 atom supercell configurations containing different numbers of (Cu_{Zn}, Zn_{Cu}) defects in various arrangements.[89] A linear correlation was found between bandgap reduction and formation energy of the defect arrangements.

Finally, a recent study gives a theoretical framework to explain optical bandgap changes as a function of temperature, in relation to Cu and Zn exchanges in kesterite material. Monte-Carlo simulations indicate a change in local coordination environments (2Cu, Zn and Sn surround each S in the ideal kesterite structure) of around 200 °C, which would be accompanied with a narrowing of the bandgap that matches very well the experimental observations.[96]

5. New Data on the Order/Disorder Effect in CZTSSe Devices

5.1. V_{oc} and Overall Performances of CZTSSe Devices

In order to gain some insight into the influence of the O/D on the V_{oc} deficit in our CZTSSe devices, we have prepared solar cells with either standard or slow cooling after the selenization step. The former series with standard cooling are hereafter labeled "PD" for partially disordered, and the latter "PO" for partially ordered. As illustrated in **Figure 8**, an increase in V_{oc} of about 40 ± 10 mV was systematically observed for devices based on slow cooling ("PO" samples). This notable increase was accompanied with a slight decrease in the short circuit current density of about 1.8 mA cm^{-2} on average. A first approximation of the IQE (calculated as IQE = EQE/(1–R), where R is the reflectance of a complete device) indicates that the decrease in J_{sc} stems from an increase of the optical bandgap (**Figure 9**), as expected from Section 4.2. By performing a linear fit (not shown here) of the plot using the following equation

$$\left[h\nu \ln\left(1-IQE\right)\right]^2 = a + b h\nu \quad (2)$$

where a and b are fitting parameters, h Planck's constant, and ν the frequency of the light, we could extract the respective bandgap values ($E_{g\text{-}IQE} = -b/a$) of the PO and PD samples: We have found a difference in $E_{g\text{-}IQE}$ of about 50 meV, the PO sample having the larger bandgap. These results are in accordance with the ones reported recently for pure Se co-evaporated CZTSe devices.[88]

In order to verify that these changes in V_{oc} and $E_{g\text{-}IQE}$ originate genuinely from the difference in crystalline order and not from altered front or back junctions, we have evaluated the optical absorption of PO and PD films lifted-off from their Mo/glass substrates. A second set of bandgap values, noted $E_{g\text{-}abs}$, was thus derived from these optical measurements. They were found to agree very well with the ones obtained by the IQE approach, thereby confirming that the bulk optical bandgap of PO samples is consistently larger (1.25 eV) than that of PD samples (1.20 eV), as summarized in **Table 2**.

Thus, ordering our CZTSSe by slow cooling after the selenization step allowed us to increase the V_{oc} of our devices by 40 meV because the bandgap of the photoactive materials increased by 50 meV. In other words, the V_{oc} deficit

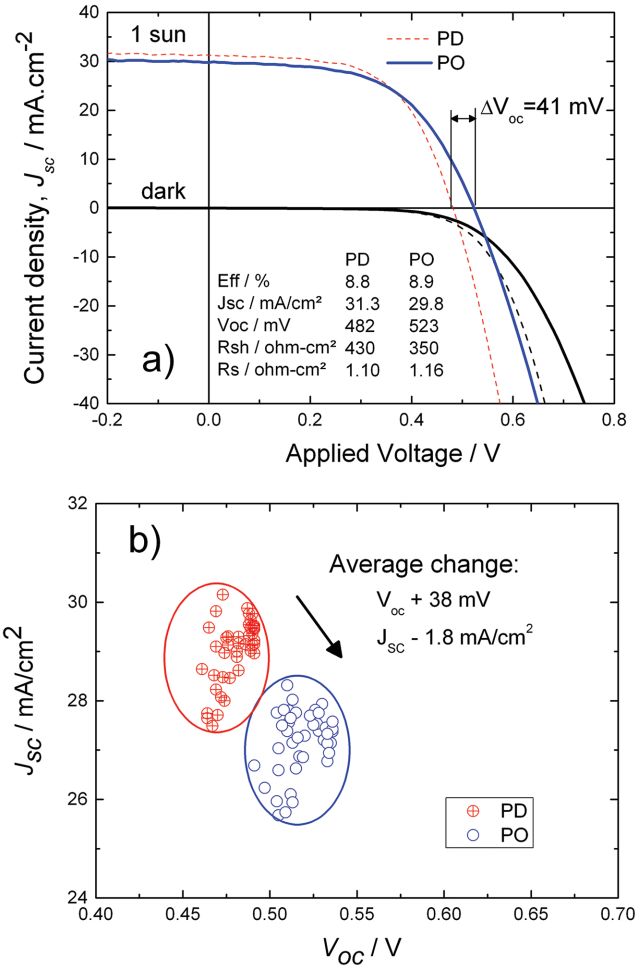

Figure 8. a) Current-Voltage characteristics under 1 sun illumination of PD (partially disordered) and PO (partially ordered) CZTSSe-based photovoltaic devices. b) Set of J_{sc}-V_{oc} data points obtained from one batch of solar cells (without ARC).

limiting the performance of our devices was not improved. This is illustrated on Figure 1, where the green points corresponding to the present study form a line parallel to the $V_{oc\text{-}deficit}$ lines. Quite recently, Krämmer et al. reported similar results on pure Se devices,[92] in which the V_{oc} exactly follows the bandgap variations (by up to 80 meV) upon reversible ordering (by slow-cooling) or disordering (by quenching after annealing at $T > T_c$).

Interestingly, capacitance-voltage (C–V) measurements performed on our PO and PD devices revealed that PO samples feature a significantly lower density of free carriers of 0.5–1 × 10^{16} cm^{-3} versus 1.5–2 × 10^{16} cm^{-3} for PD samples. This lower carrier concentration in PO samples can explain the enhanced quantum efficiency visible in Figure 9 between 600 and 900 nm, by an extension of the space charge region (SCR) deeper in the CZTSSe layer. Very similar trends have been observed in pure selenide devices.[97] The collection length in these less doped PO layers becomes more voltage-dependent since it has a larger contribution of the SCR width with respect to the diffusion length than the PD samples. This effect causes a voltage-dependence of the photocurrent and hence a reduced

© 2016 WILEY-VCH Verlag GmbH & Co. KGaA, Weinheim

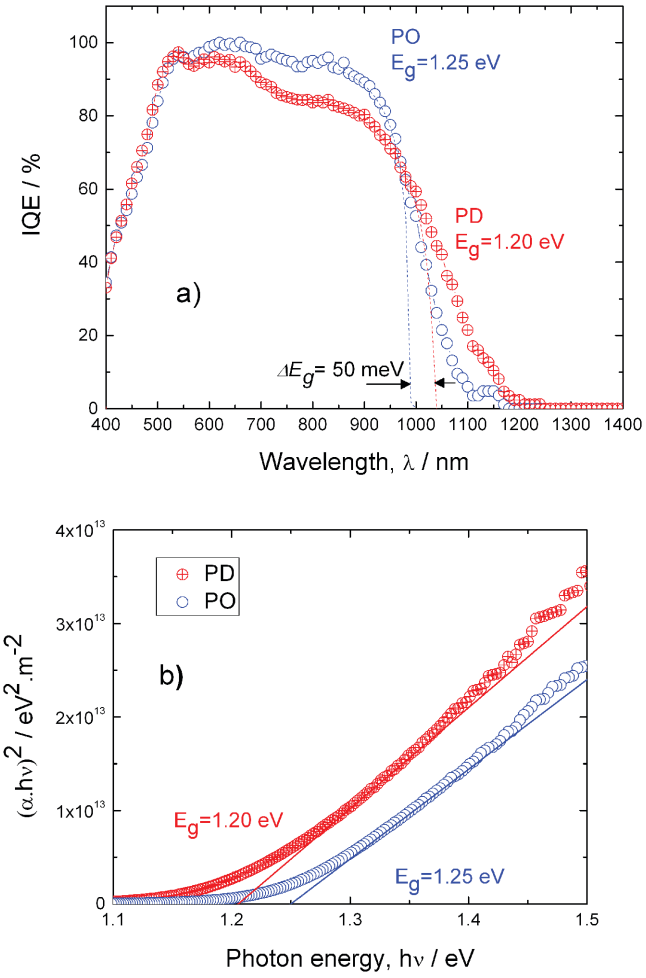

Figure 9. a) Internal quantum efficiency (IQE) spectra of CZTSSe-based photovoltaic devices of PD (red symbols) and PO type (blue symbols). The dotted lines correspond to fitted IQE according to Equation (2) in the range used to extract $E_{g\text{-IQE}}$. b) Linear fit of $(h\nu\alpha)^2$ vs photon energy $h\nu$, based on the absorption coefficient α measured on lift-off samples from the same batch; used to derive $E_{g\text{-abs}}$ (same colors).

fill factor. This point may become important in the future, if devices based upon ordered layers will have to be optimized.

5.2. Role of Anionic Disorder in CZTSSe

As mentioned above (Table 1), the best kesterite devices achieved to date are based upon CZTSSe photoactive layers comprising both S and Se. Since CZTS and CZTSe kesterites have bandgaps that are 500 meV different, one may legitimately ask whether a potential inhomogeneous spatial distribution of S and Se anions could occur, and what would be its implication as far as V_{oc} deficit is concerned.

As a matter of fact, S and Se are known to have only a small size and chemical mismatch. By employing the special quasi-random structure approximation, Chen et al. have shown that the isovalent CZTSSe alloy is very well behaved and can be described by the regular solid solution model (as confirmed experimentally by a fully respected Vegard's law)[101] with an interaction energy of 26 meV per atom.[95] This suggests that the homogeneous alloy is stable for this system at the typical growth temperatures. The same authors concluded from ab initio calculations that the optical bandgap of $CZTS_xSe_{(1-x)}$ alloys follows the relationship

$$E_g(x) = xE_{g\text{-CZTS}} + (1-x)E_{g\text{-CZTSe}} - bx(1-x) \quad (3)$$

where $E_{g\text{-CZTS}}$ = 1.5 eV is the bandgap of pure sulfide CZTS, $E_{g\text{-CZTSe}}$ = 0.96 eV the one of pure selenide CZTSe, and b = 0.1 eV is the so-called bowing coefficient, independent of the composition. This simple relationship was verified experimentally[16,98] thereby confirming the assumption of a homogeneous distribution of anions within the photoactive layer.

It should be underlined though that the alloy model proposed by Chen et al. refers to a system in complete thermodynamic equilibrium. For a CZTS sample that is subsequently annealed in Se (vast majority of the CZTSSe cases), the situation could be quite different depending on the annealing temperature and time. Indeed, a compositional gradient of the two anions could be expected at the surface and at grain boundaries because of kinetic effects. Due to the slow solid-state diffusion process, a higher concentration of Se could occur at the exterior, while the interior of the grains would remain higher in S concentration. In order to verify this hypothesis, we have investigated the local anionic distribution by carrying out STEM-EDX analysis on several CZTSSe thin film slices. **Figure 10**a and b represent line scans performed within individual grains, and starting from the top surfaces.

Depending on the analyzed area, the cation and anion compositions can be found to be rather stable, as in Figure 10a. In other locations such as that of Figure 10b, the concentration of Se seems to decrease by more than 5% with increasing depth. This latter case thus confirms the hypothesis proposed above and is based upon a slow solid-state diffusion of Se within CZTS grains during the selenization process. We have extended this TEM study by investigating the grain-to-grain variation of the anion ratio. Figure 10c shows the chemical composition of 24 different grains located within slides extracted from the same equivalent samples showing efficiencies higher than 10%. One can note that the anionic ratio x = S/(S+Se) varies

Table 2. Summary of E_g and V_{oc} values measured on typical PO or PD samples.

Structure	$E_{g\text{-abs}}$ [eV]	$E_{g\text{-IQE}}$ [eV]	V_{oc} [V]	V_{oc} deficit [V]		N_{cv} [cm^{-3}]	E_g-E_{PL} [meV]
Partially ordered, PO	1.25	1.25	0.523	0.73	58%	5×10^{15}	150
Partially disordered, PD	1.20	1.20	0.481	0.71	59%	2×10^{16}	165
Difference Δ	0.06	0.05	0.04	0.02			15

© 2016 WILEY-VCH Verlag GmbH & Co. KGaA, Weinheim

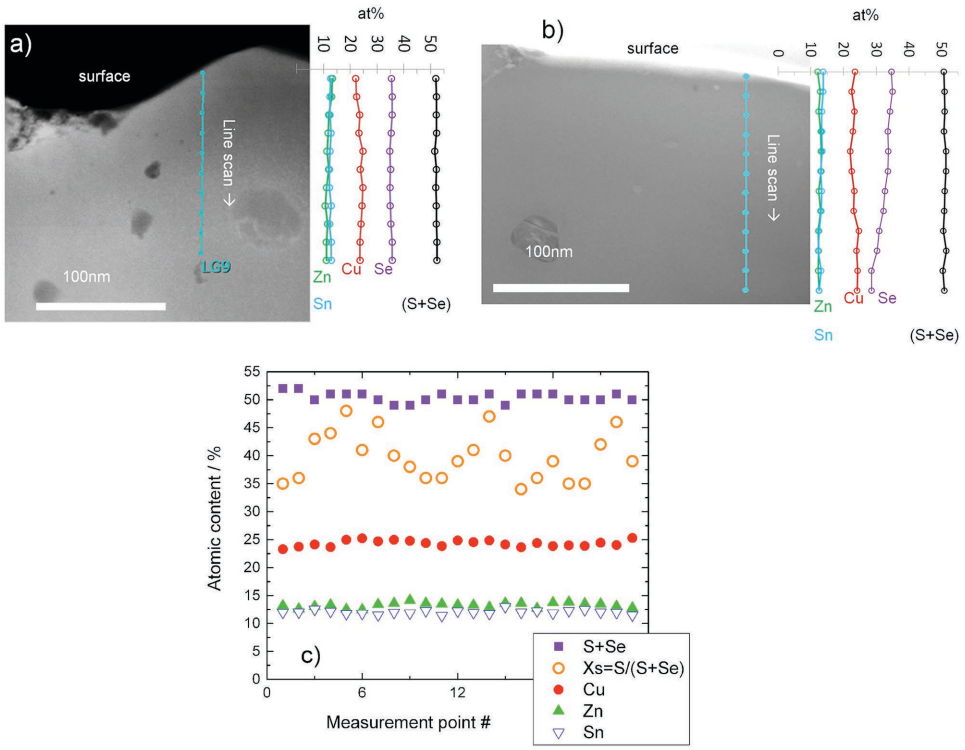

Figure 10. Cross-section STEM-EDX compositional analysis of standard CZTSSe absorber thin films. Line scans in grain with a) uniform and b) non uniform composition. c) Grain-to-grain variation evaluated from 24 data points measured on various grains from a few sections, with 1 data point per grain.

between x = 0.34 to x = 0.48 thus yielding a local amplitude on x as large as ± 0.07. These high grain-to-grain variations in the anionic composition of CZTSSe films, also observed by Roelofs et al.,[99] are believed to be genuine. However, it would be rather difficult to extract a reliable and accurate average distribution of the anionic compositions from such local TEM measurements. For that matter, XRD measurements are better suited.

Figure 11a displays the grazing angle XRD patterns measured on various CZTSSe/Mo/glass thin films with anionic concentration varied from x = 0 (pure selenide CZTSe) to x = 1 (pure sulfide CZTS). The fabrication details can be found in the experimental section. All samples have been annealed and finally cooled in the same, standard "fast" cooling conditions. A close look at the dominant (112) peak clearly shows the typical peak-shift towards higher diffraction angles 2θ when increasing the S content (Figure 11a). Importantly, these peaks can be well distinguished thanks to low full width at half maximum values (FWHM about 0.15°), typical of rather narrow and homogeneous composition distribution. A slight asymmetry with an apparent shoulder on the low 2θ angle side is visible in all cases

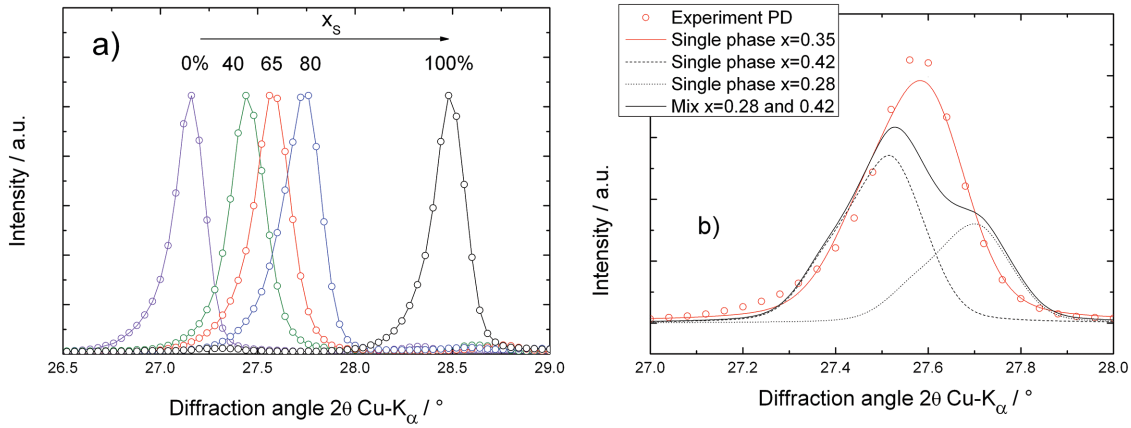

Figure 11. XRD patterns of CZTSSe/Mo thin films with focus on (112) peaks. a) Variable samples with anion ratio x = S/(S+Se) varied from 0 to 100%. b) Full pattern matching results for PD type of sample (i.e., standard sample, red open dots) using a single kesterite phase (x = 0.35) and another fitting example with two mixed phases x = 0.28 /0.42 with volume fractions of 63%/37%.

© 2016 WILEY-VCH Verlag GmbH & Co. KGaA, Weinheim

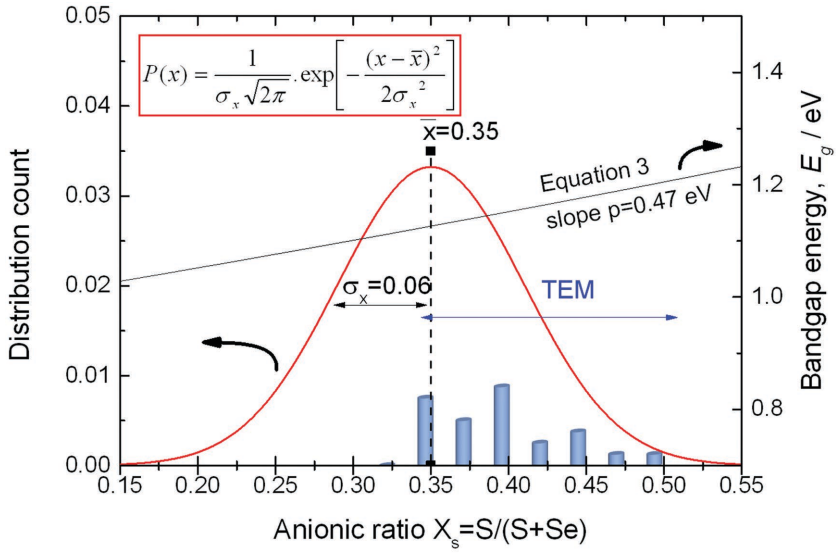

Figure 12. Composition distribution of anion ratio x = S/(S+Se) in our standard CZTSSe films, centered on x = 0.35 as derived from XRD and with standard deviation σ_x = 0.06 overestimated, compared with full pattern matching (e.g. Figure 11b). The blue bars are the indicative distribution measured by TEM (Figure 10c). The black line corresponds to a theoretical bandgap calculated using Equation (3), the slope of which (p = 0.47 eV around x = 0.35) is used to derive $\sigma_{Eg} = p.\sigma_X$.

(Figure 11b), which is not related to composition distribution, but rather to a typical effect of the θ–2θ diffraction setup,[100] especially visible on the low diffraction angles, such as $2\theta \approx 27°$. We have conducted a unit cell refinement (through the full pattern matching mode) on a standard sample, assuming a unique composition (Figure 11b) leading to average lattice parameters a = 5.6084(6) Å and c = 11.1711(5) Å. According to the linear variation of the tetragonal unit cell parameters within the solid solution $Cu_2ZnSn(S_xSe_{1-x})_4$,[101] these values correspond to a sulfur content close to x = 0.35.

In order to appreciate whether such XRD signal could stem from a mixture of two distinct phases having different anionic compositions, we have tried to fit the 112 peak shown on Figure 11b by assuming such mixture of 2 phases (S-poor and S-rich) having an average composition close to 0.35 for 2 cases, namely x = 0.28/0.42 and x = 0.34/0.48. For x = 0.28/0.42 the two phases (dotted line of Figure 11b) give 2 distinguishable peaks clearly not seen on the experimental pattern. On the other hand, the second fit with x = 0.34/0.48 leads to phase volume fractions of 99.1%/0.9% (not shown on Figure 11b because almost superimposed on the single phase fit curve). We thus conclude that the sample is made of CZTSSe with an average composition of x = 0.35 ± 0.05.

From this result, we assume a Gaussian distribution for the anionic composition x = S/(S+Se) centered on x = 0.35 (**Figure 12**). In order to account for the variations detected by TEM analysis (as summarized in Figure 10), we derive a standard deviation σ_x = 0.06 that will be used in the next section. We note that the few points detected by STEM-EDX at x = 0.35 correspond to measurement area in large grains: Their large volume yields a STEM-EDX value close to the one derived from XRD. On the other hand, small grains appear richer in S; this can match the interpretation anticipated from theory that selenization proceeds from diffusion along grain boundaries towards inside of the grains. Thus, this combined STEM and XRD investigation has revealed that although the photoactive layer is made of a dominating phase having a well-defined anionic mixture, some small grains do have a quite different anion composition. This opens the question of the potential impact of this variation upon the V_{oc} deficit at work in CZTSSe kesterite photovoltaic devices.

5.3. Potential Impact of the Anionic Disorder on V_{oc} Deficit

The maximum AM1.5G efficiency of a single junction solar cell based on a perfect 1.2 eV bandgap absorber and calculated within the framework of Shockley-Queisser (pure radiative recombination)[102] is η_{max} = 31.6%. The theoretical V_{oc} calculated under these assumptions reaches 0.940 V, representing a V_{oc} deficit of 0.260 V.

In order to account for the potential bandgap fluctuations described by a Gaussian distribution with a standard deviation σ_{Eg}, Rau et al. have proposed the following equation:[61]

$$V_{oc} = \frac{E_g}{q} - \frac{\sigma_{Eg}^2 q}{2k_B T} - \frac{k_B T}{q} ln\left(\frac{J_{00}}{J_{sc}}\right) \quad (4)$$

where E_g is the bandgap, q is the elementary charge, k_B is the Boltzmann constant, T is the temperature, J_{00} is the pre-exponential factor of the dark saturation current density, and J_{sc} the short circuit current density under AM1.5G.

The distribution of the anion ratio x = S/(S+Se) quantified in Section 5.3 and illustrated on Figure 12, can be tentatively translated into a distribution of bandgap using Equation (3). Following this line of thought, the normal anion distribution centered on x = 0.35 with a standard deviation σ_x = 0.06 suggests a normal distribution of bandgap centered on E_g = 1.20 eV (as measured optically) with a standard deviation σ_{Eg} = 0.028 eV. Note that Equation (3) gives a theoretical bandgap of $CZTS_xSe_{(1-x)}$ compounds with stoichiometric composition and with perfect Cu/Zn order (black line in Figure 12), therefore noticeably different (here smaller) than that found experimentally in our Cu-poor, Zn-rich PD samples. From Equation (3) we used only the slope p of the curve around x = 0.35. Applying this σ_{Eg} number to Equation (4), we calculate a theoretical V_{oc} of 0.914 eV. This value is actually very close to the V_{oc} calculated by assuming no bandgap fluctuation at all (0.940 V). We can thus safely conclude that the bandgap fluctuations related to the inter-grain anionic distribution in our CZTSSe samples at macroscopic scale (>>1 µm–10 cm) is very unlikely to play a significant role in the overall V_{oc} deficit harming our devices.

One may argue that the model used above assumes a locally homogeneous material, and does not account for the situation

© 2016 WILEY-VCH Verlag GmbH & Co. KGaA, Weinheim

Table 3. Calculated impact of the anion composition x = S/(S+Se) distribution on the maximum photovoltaic parameters within the SQ-limit, based on absorber bandgap centered at 1.20 eV. The mix assumes small grains with two equi-volumetric populations of grains with x = 0.25 and 0.45, i.e. E_g = 1.24 and 1.14 eV, respectively.

Composition	E_g [eV]	η [%]	J_{sc} [mA cm^{-2}]	FF [%]	V_{oc} [V]	ΔV_{oc} [V] (% of E_g)
Uniform	1.14	32.3	41.3	87.2	0.896	0.244 (21.4)
	1.20	31.6	38.4	87.6	0.939	0.251 (21.0)
Mix	1.24	31.6	36.4	88.1	0.983	0.254 (20.5)
	1.19	28.0	36.4	87.3	0.910	0.280 (23.5)

where the intra-grain composition is different. In order to study that very case, let us assume that our active layer is made of small grains (<<1 µm) with two distinct compositions, each representing an equal volume fraction of 50% of the photoactive film. Furthermore, let us assume that their anionic compositions are x = 0.25 and 0.45 (that translates into bandgaps of 1.14 eV and 1.24 eV, respectively). We stress that these hypothesis are not realistic as explained in Section 5.4 (as such case would have been detected by XRD), and hence represent a worst case scenario. However, following the approach used by Djemour et al.,[103] one can estimate the maximum theoretical V_{oc} (Shockley-Queisser conditions) of such a photoactive mixed material by postulating that:

- J_{sc} is dictated by the largest bandgap of the two phases
- J_0 of the mixed material is given by the arithmetic sum of the volumetric contribution of the different phases, since each phase can emit its black body radiation in a mixed 3-dimensional arrangement.

These assumptions yield a maximum theoretical V_{oc} of 0.910 V, which is only 30 meV lower than in the case of a homogeneous photoactive layer having a bandgap of 1.2 eV (**Table 3**). Thus, we hereby conclude that only a very negligible fraction (less than 2.5%) of the V_{oc} deficit can be attributed to spatial bandgap fluctuation stemming from anion non-uniformity at the small scale (<<1 µm).

The very same two approaches can be applied to evaluate the potential impact of the Cu/Zn disorder upon the V_{oc} deficit. Let us assume that for a given anion ratio, the bandgap of the photoactive absorber can vary by about 150 meV between the fully ordered and disordered states (see section 5.5). Considering an even distribution of these bandgaps, a standard deviation of $\sigma = 150/4 = 0.038$ eV seems reasonable. Applying this number to Equation (4), one concludes that the maximum potential V_{oc} deficit induced by the Cu/Zn disorder is only of 47 meV. The grain-to-grain variation model used above gives about the same magnitude. Thus we can conclude that the bandgap fluctuation induced by the Cu/Zn disorder cannot explain the majority of the V_{oc} deficit harming kesterite solar cells.

5.4. Radiative versus Non-Radiative Recombination

In order to find out whether the crystalline disorder at work in CZTSSe has any impact upon the balance between radiative and non-radiative recombination, we have characterized our samples using cathodo-luminescence (CL). We have first measured CZTSSe thin films (without a CdS buffer) fabricated with the same thermal protocol used for the PO and PD samples discussed in Section 5.1. The results are shown on **Figure 13**a. Clearly the CL peak position of the PO sample is shifted to a larger energy by about 60 meV, what is consistent with the difference in optical bandgap between PO and PD layers reported above and summarized in Table 2. The CL intensity is found also larger in the PO sample, indicative of more radiative recombination. It should be noted that we did not observe any CL interference effect, contrarily to what has been reported in standard photoluminescence measurements carried out in CZTSe films.[103,105] We believe that this can be explained by the notable roughness of our samples. Nevertheless, some systematic artifacts appeared at 0.94 and 1.09 eV (Figure 13), presumably due to parasitic absorption losses within the CL set-up.

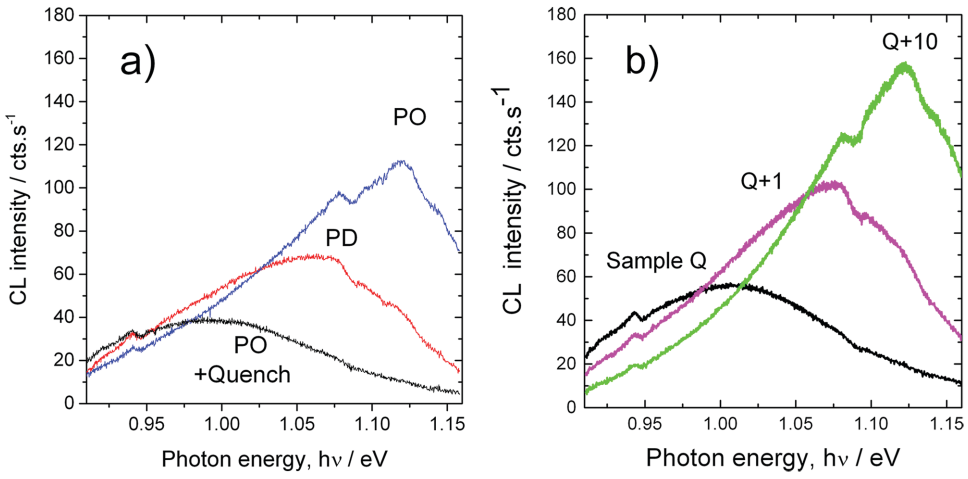

Figure 13. Cathodo-luminescence of CZTSSe layers a) (PO) partially ordered vs (PD) partially disordered samples similar to those used in devices of Figure 8, 9. b) (Q) quenched after a 60 min annealing at 300 °C, (Q+1) quenched and further annealed at 100 °C during 24 hours, and (Q+10) quenched and further annealed at 100 °C during 240 hours.

© 2016 WILEY-VCH Verlag GmbH & Co. KGaA, Weinheim

In order to further confirm these CL results, we have prepared a second series of samples using our standard process, in which we varied the O/D by applying various post-annealing processes. All samples were heated under nitrogen at 300 °C for 60 min and quenched from there (noted "Q") in order to induce complete disorder (see Figure 7). The samples were then further annealed under nitrogen at 100 °C for 0 (Q), 1 (Q+1) and 10 (Q+10) days respectively, in order to induce some controlled ordering. Figure 13b displays the corresponding CL spectra collected on each type of samples. The trends shown on Figure 13b appear comparable and consistent with those visible on Figure 13a, both in terms of peak positions and intensities. One can note that the CL emission peak shifts by more than 100 meV towards larger energies with increasing annealing time at 100 °C. Considering that the lowest energy CL peak in Figure 13b ($E_{CL,D}$ = 1.01 eV) corresponds to the fully disordered state (S = 0, quenched from T ≥ T_C) and that the highest energy CL peak ($E_{CL,T=100}$ = 1.12 eV) corresponds to the most ordered state achievable at 100 °C (see Figure 7), one can estimate the order parameter reached at 100 °C using the following equation

$$\frac{T}{T_c} = \frac{2S(T)}{ln\left(\frac{1+S(T)}{1-S(T)}\right)} \quad (5)$$

where T is the temperature at which the sample has been ordered (here 100 °C), T_C, the critical temperature of the O/D transition ($T_C \approx$ 200 °C), and $S(T)$ the order parameter achieved at equilibrium and at the temperature T. Solving Equation (5) for T = 100 °C yields S = 0.72.

Besides, postulating that,

$$S(T) = \frac{E_{CL,T} - E_{CL,D}}{E_{CL,O} - E_{CL,D}} \quad (6)$$

where $E_{CL,O}$ is the energy of the CL peak for a fully ordered sample (S = 1, at T = 0K), one can calculate using the values extracted for T = 100 °C that $E_{CL,O}$ = 1.16 eV. Thus, this interpretation of the CL data suggests that the bandgap variations from fully disordered (T > T_C) to the most ordered state at ambient conditions could be as large as 150 meV, that is about 15% of the bandgap of the disordered state.

Beyond confirming the large impact of O/D upon the bandgap of CZTSSe, Figure 13 reveals notable new information. The blue shift in the CL peak position is accompanied with a significant increase in the intensity of the CL signal by nearly a factor 3×. This appears quite promising since a direct correlation exists between luminescence yield, minority carrier lifetime, and device efficiency.[28] We verified also that a factor 2.5× was still present when measured on a series of similar CZTSSe samples coated with a CdS buffer on top (as is the case in complete solar cells devices). This indicates that any change of the space charge region width, anticipated to modify the CL emitting volume, has actually weak influence on CL intensity and on this ratio. These experiments performed in otherwise identical conditions, point to changes in materials radiative bulk property.

An obvious tentative explanation would be the positive impact of the reduction of the number of point defects in the CZTSSe crystal, especially (Cu_{Zn}+Zn_{Cu}). However, one could potentially also invoke a passivation of the grain boundaries by the creation of an oxide layer as shown under other circumstances,[12] or a redistribution of Cu, as observed recently.[106] In order to verify the likeliness of these hypotheses, we have tested the reversibility of the effect observed on Figure 13. It appeared that a PO sample further heated at 300 °C for 60 min and quenched from there (Figure 13a) shows about the same peak position and CL yield than a Q sample (Figure 13b). This reversibility tends to discard the explanation based upon the passivation of grain boundary, and reinforces the one invoking the reduction of the number of point defects.

From the literature, the CL efficiency of electron-hole pair generation (EHP) is inversely proportional to the bandgap energy E_g of the material measured:[107] Hence the blue-shifted sample, having larger bandgap by ≈10% should result in a reduced CL yield. Assuming otherwise identical parameters, this would correspond to a reduced CL intensity, which is the opposite of what we observe. Thus, we tend to attribute the actual rise in CL intensity observed in Figure 13 to a genuine increase in radiative recombination.

Actually, the intensity of light, I_L emitted by radiative recombination of injected EHPs can be expressed as a function of the photon energy, $h\nu$:[70]

$$I_L(h\nu) = \frac{2\pi}{h^3c^2}\left[1-\exp\{-\alpha(h\nu)d\}\right] \times \frac{(h\nu)^2}{\exp\left(\frac{h\nu-\Delta\mu}{k_BT}\right)-1} \quad (7)$$

where the emissivity of the material (the second term in brackets) is multiplied by the volumetric-based internal spontaneous emission from band–band transitions. Under irradiation, the density of EHPs is reflected in $\Delta\mu$, the amplitude of the quasi-Fermi level splitting (QFLS). Obviously, the higher $\Delta\mu$, the larger I_L. When considering the absorption coefficient of a direct gap semiconductor, simply expressed as $\alpha(h\nu) = \frac{A}{h\nu}[h\nu - E_g]^{1/2}$ and using fixed $\Delta\mu$, T and A parameters, simulations from expression (7) indicate that i) the luminescence spectrum is blue shifted when increasing the bandgap E_g (as anticipated) but as well that ii) I_L reduces in intensity. This again is in opposition to our experimental observations, indicating that the actual $\Delta\mu$ is larger when E_g is increased through ordering. Interestingly, assuming that the increase in E_g is accompanied by an equivalent increase in $\Delta\mu$ (for instance, taking E_g and $\Delta\mu$ increasing from 1.15 to 1.25 eV and from 0.6 to 0.7 eV, respectively) yields an increase in I_L, yet this is rather small (less than 20%) compared with the 1.6× ratio seen experimentally from PD to PO sample cases. In summary, even though a more complete optical model including sub-gap absorption[70] may be necessary to extract all the information comprised in Figure 13, the observed increase of both CL peak energy and intensity indicates that the absorber's bulk radiative properties of the ordered kesterite type are significantly improved, with the possibility that the entire rise in bandgap (and even more) would translate in QFLS. Further investigations are needed to confirm this latter point.

6. Concluding Remarks and Perspectives

It is has been now largely evidenced that CZTSSe undergoes a structural transition at a temperature T_C close to 200 °C. The

© 2016 WILEY-VCH Verlag GmbH & Co. KGaA, Weinheim

transition has been attributed to the exchange of Cu^{+} and Zn^{2+} cations located at the *2c* and *2d* Wyckoff sites of the kesterite structure, respectively. At temperatures above T_C (disordered state), kesterite can have a bandgap up to 150 meV smaller than the one it would have in its fully ordered state.

Tuning of the O/D degree in efficient ($\eta \geq 9\%$) devices allowed us to show that the V_{oc} deficit is not reduced in these solar cells when the order is enhanced. The V_{oc} appears higher because the bandgap of the photoactive materials is larger. This latter point explains as well that i) the J_{sc} is notably reduced, and that ii) the overall efficiency remains equivalent. Moreover, using two different models applied within the Shockley-Queisser detailed balance approach, we came to the conclusion that potential inter- and intra-grain bandgap fluctuations induced by a speculative distribution of order degree within a same layer (both Cu/Zn disorder or S/Se distribution), would have no significant effect upon the V_{oc} of the devices. Thus, the effect of disorder in the Cu/Zn sub-lattice seems to be rather negligible at the level of performances at which state-of-the-art kesterite solar cells stand today. Interestingly, our cathodo-luminescence measurements indicate that ordered kesterite crystals should be preferred because the intensity of radiative recombination of charge carriers is found to be significantly larger. Nevertheless, only a minor fraction of this potential improvement is apparently translated via the QFLS into the V_{oc}.

6.1. Urbach Tails

One known mechanism of non-radiative recombination occurs via band tails present at the edges of the conduction and valence bands of a semiconductor. This can be quantified by the Urbach energy, E_u, which appears larger in defective and/or disordered materials such as amorphous silicon. Recently, De Wolf et al. proposed a direct link between E_u and V_{oc} deficit in standard photovoltaic materials. The red points of **Figure 14**a correspond to the lowest E_u and lowest reported V_{oc} deficit values for various types of solar cells.[76] We have added on this plot the few data available in the CZTSSe literature. From this plot, CZTSSe devices are again distinct from other photovoltaic materials by their larger V_{oc} deficit. Another way to look at this issue is represented on Figure 14b, where this time E_u is plotted versus E_g. This latter graph suggests that E_u does increase naturally with E_g, thus implying that ordered kesterite should have larger Urbach tails than disordered kesterite. Some discrepancy can be observed among data, likely because the measurement methods as well as the analysis approaches used to extract E_u can differ significantly. More exhaustive measurements are required, in order to assess the potential impact of Urbach tails in kesterite devices.

So far, we have characterized band tailing in our PO and PD samples only by studying the red shift E_g–E_{PL} between the optical bandgap energy and the peak energy position of photoluminescence spectra. We have found very close values of 165 meV and 150 meV for PD and to PO type of samples, respectively (Table 2). Provided that we have measured an E_g–E_{PL} of less than 80 meV in high performance CIS samples, we conclude that O/D has only a minor impact upon the large shift between PL and absorption occurring in our CZTSSe samples. One should keep in mind though that a fundamental limitation arises when investigating the impact of the Cu/Zn order on CZTSSe, namely the actual impossibility of varying the order parameter S up to S = 1, because of basic thermodynamic reasons. As seen above, this parameter can be tailored at room temperature from S = 0 (fully disordered CZTSSe) to S = 0.72 in our case, or even up to 0.8 reported recently in sulfide CZTS material,[18] but never above S = 0.9. Increasing S from 0 to S = 0.8 is equivalent to reducing $D_{[CZ]}$ ($D_{[CZ]}$ is the number of (Cu_{Zn}+Zn_{Cu}) defect pairs in each conventional kesterite unit cell; linked to S via $D_{[CZ]} = 1–S$)[89] from 1 down to 0.2. This translates in a reduction of this defect density by a factor 5 only, that is from 3×10^{21} cm^{-3} (for S = 0) down to 6×10^{20} cm^{-3} (for S = 0.8). We believe that the Cu/Zn disorder may be reduced much more significantly by altering the CZT elemental composition. Indeed, as already mentioned in Section 2.5, partial elemental substitution of either Zn (e.g., with Cd)[18] or of Cu (with Ag)[54] have been reported to yield a sharper absorption edge, indicative of a reduced band tailing. Here again, further investigations of the red shift and of E_u versus O/D in these specific materials would be beneficial for the overall comprehension of the V_{oc} deficit at work.

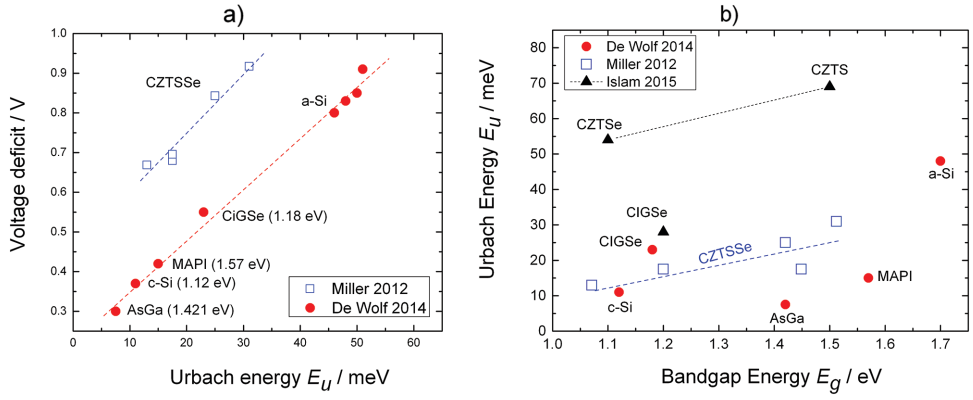

Figure 14. a) Relationship between Urbach energy E_u and lowest reported voltage deficit, for various photovoltaic materials, after De Wolf et al.[76] Data available from Miller et al.[75] and Islam et al.[63] were included.

© 2016 WILEY-VCH Verlag GmbH & Co. KGaA, Weinheim

6.2. Deep Defects

As indicated on Figure 2 (bottom), Sn_{Cu} (+/2+), Sn_{Cu} (2+/3+), and Sn_{Zn} (+/2+) point defects yield deep states in the band gap. Recently Yee et al.[81] estimated computationally that the concentration of such deep point defects can reach values up to 10^{16} cm^{-3} (Sn_{Zn}) in Cu-poor, Zn-rich CZTSe material processed at 800 K. Because the donor defect Sn_{Cu} (+/2+) has a transition level of E_v+0.35 eV (i.e., quite close to E_F and below midgap), it is estimated to be particularly harmful, even in small concentrations (>10^{10} cm^{-3}). Therefore, both Sn_{Zn} (+/2+) and Sn_{Cu} (+/3+) are likely to be efficient recombination centers for electrons. Moreover, these defects can actually form clusters with the omnipresent Cu_{Zn} and Zn_{Cu} defects involved in the Cu/Zn order, which can increase significantly their potential density. For example, the cluster ($2Cu_{Zn}$, Sn_{Zn}) has the lowest enthalpy of formation, besides of course (Cu_{Zn}+Zn_{Cu}) (see top of Figure 2). In order to reduce the probability of presence of these harmful deep defects, growing films in Sn-poor conditions (but not too much, as already seen in Section 3.2)[15] can be highly beneficial.

Another source of deep defects to be considered is, naturally, the grain boundaries. As discussed in Section 2.2, some passivation treatments have been shown to be very effective in certain instances. This observation is further supported by the quasi systematic improvement of the photovoltaic parameters when the grain size is increased through the usage of fluxing agents (Section 2.5). In 2013, Xu et al.[108] calculated the energy levels of defects potentially present at the (112) surface of CZTSSe: They found that the cluster (Cu_{Zn}+Cu_{Sn}) is located very close to the midgap in stoichiometric material and may thereby be harmful; they conclude that Cu-poor growth conditions are preferred. Nevertheless, as this superficial cluster defect involves the omnipresent Cu_{Zn} defect, we anticipate that Cu/Zn (dis)ordering might play a role in its density and recombination activity. Furthermore, more recent calculations of defects at the Σ3 (114) grain boundary of CZTSe have indicated that Cu–Sn and Se–Se wrong bonds could generate three energy levels located within the bandgap and thus act as effective SRH recombination centers.[104,109] This further suggests that the grain boundaries of kesterite are likely to be rather electrically active, and as such deserve some additional specific studies.

Finally, further progress in CZTSSe could be inspired from methods used in parent thin-film CIGSe and CdTe technologies such as bandgap grading, and conduction band offset optimization using alternative buffers both at the front and back interfaces.

7. Experimental section

CZTS layers were deposited on Mo glass substrates by non-pyrolytic spraying inside a N_2 glove box, using an additive-free water-ethanol (90–10%vol) based ink of a Cu–Zn–Sn sulfide (no Se) colloid with ≈10 nm primary particles size. This ink is obtained at room temperature by instantaneous precipitation reaction between two solutions (one of NaHS dissolved in de-ionized water and the other of Cu, Zn and Sn metal chloride salt precursors dissolved in acetonitrile) followed by some washing steps and formulation in water/ethanol. The experimental details regarding the colloid synthesis, the ink preparation and the spray deposition technique can be found elsewhere.[42] The NaHS solution was in excess of 20 to 40% molar with respect to the total metal stoichiometry. The Cu/Zn/Sn cation ratio in the metal precursors was off-stoichiometric.

Our standard CZTSSe films were used for photovoltaic devices, lift-off films and CL characterization. For that, pure sulfide CZTS colloids with Cu/Zn/Sn cation content of 1.7/1.1/1 (equivalent to 45.25/28.5/26.25 at%) were spray-deposited and then annealed using a two-step annealing: A first annealing step in an inert (N_2) atmosphere allowed the growth of the precursor particles from nanometer up to micrometer size. The second annealing step in the Se vapor-containing atmosphere allowed both the incorporation of Se (partially replacing the S) and the curing of the secondary phases present after the first annealing step.[43] The cooling applied at the end of the selenization step of our standard process (PD samples) was not close-loop controlled: The samples cooled naturally from 550 °C to 130 °C within 2 hours typically, and from 130 °C to 40 °C in 5 to 6 hours. For slow-cooled samples (PO type), a linear slope of 10 °C h^{-1} was controlled between 350 °C down to 20 °C within 30 hrs.

For XRD analysis (Figure 11), additional CZTSSe/Mo/glass films with variable anionic ratio x = S/(S+Se) from 0 to 1 used a slightly different Cu/Zn/Sn metal precursor ratio of 1.9/1.2/1 (equivalent to 46.25/29.0/24.75 at%). The pure sulfide sample (x = 100%) was made from a sprayed film annealed under pure Nitrogen, followed by H_2S annealing.[42] The pure selenide sample (x = 0%) was made by annealing in two steps (N_2 then Se) a film sprayed from pure Se colloidal ink, while the others (x≈40, 65 and 80%) were made from mixed S/Se precursors in colloidal aqueous inks; the synthesis of which has been detailed elsewhere.[101]

Our photovoltaic devices are of "substrate" type: ITO/ZnO/CdS/CZTSSe/Mo/glass. The CdS, ZnO, and transparent conductive oxide layer (Indium Tin-doped Oxide, ITO) had thicknesses of 50 nm, 60 nm and 400 nm, respectively. Each substrate was 25 × 25 mm^2, on which 16 cells of 5 × 5 mm^2 surface area each were defined by mechanical scribing. A finger grid of Ni (50 nm) and Al (1 µm) was deposited by e-beam evaporation through a dedicated mask atop the ITO layer in order to ensure a good current collection. These steps are detailed elsewhere.[42,43]

Lift-off CZTSSe films used for optical measurements were fabricated by gluing standard CZTSSe/Mo/glass samples to flat quartz plates, followed by the application of a fast mechanical force so as to cleave the CZTSSe/quartz part from the Mo/glass substrate. The CZTSSe lift-off films remained glued to the transparent quartz substrate by the top surface, leaving the CZTSSe back surface exposed.

Transmittance T and reflectance R spectra in the 250–2500 nm wavelength range were recorded on the CZTSSe/glass lift-off samples with a UV–Vis–NIR spectrophotometer (Perkin Elmer Lambda 950) equipped with an integrating sphere (diameter 150 mm) using a photomultiplicator (250–860 nm) and InGaAs detector (860–2500 nm). The wavelength was calibrated with a deuterium lamp. The CZTSSe layer faced the light source under an incidence of 0 or 8° for T and R measurement, respectively. Knowing the CZTSSe film thickness e, as measured from SEM cross section (averaged on a few points) and neglecting the role of the glass template (which was checked transparent in the relevant wavelength range), the absorption coefficient α was derived from R and T using $\alpha = (-1/e)\mathrm{Ln}(f(R,T))$, as detailed in Vargas 2003.[110] FE-SEM (Field-Emission Scanning Electron Microscopy) images were acquired with a Hitachi S-4700 apparatus, to which an EDX (Energy-Dispersive X-ray microanalysis) Noran System SIX was coupled. Transmission Electron Microscopy (TEM) analysis was carried out with a JEOL 2100F FEG-200 kV microscope, having a Scanning TEM (STEM) accessory, and an integrated JEOL JED-2300T EDX analyzer. Thin slices were prepared by Focused Ion Beam (FIB). No forced cooling was used during EDX-STEM measurement, but we consider that local heating has negligible impact on S/Se interdiffusion or elemental loss because of the scanning mode used. We double checked that the S/Se element distribution from grain-to-grain was also observed on EDX-STEM

© 2016 WILEY-VCH Verlag GmbH & Co. KGaA, Weinheim

images with lower magnification. XRD (X-ray Diffraction) was measured with a Brüker D8 Advanced diffractometer using Cu Kα radiation and grazing incidence, typically at 1° and 3°. Current–voltage (I–V) curves were recorded with a Keithley 2601 Source Measurement Unit and an AAA-class solar simulator (Oriel Sol3A, from Newport). The external quantum efficiency (EQE) was measured from 400 to 1400 nm with an in-house setup using chopped monochromatic light, lock-in detection, and no white light bias. The internal Quantum efficiency IQE was calculated as IQE = EQE/(1–R), where R is the reflectance of a complete device. C–V measurements at room temperature were carried out with an E4980A LCR meter operating in capacitance-conductance (CPG) mode in the frequency range from 100 Hz to 1 MHz. During the whole measurement, the solar cells were kept in the dark; the DC bias was varied from –0.6 V to +0.6 V with an AC voltage of 30 mV. We derived the capacitance (C) by applying an equivalent circuit model comprising a capacitor in parallel with a resistor as proposed by Scofield et al.[111] This allowed us to extract the charge carrier density, N_{CV}, versus the distance to the front interface, *x*, at a given frequency, following the formalism proposed by Miller et al.[112] From the typical U-shape of those $N_{CV}(x)$ curves (where x is the so-called "distance to the junction") we have extracted the values of the minimum in the plateau as the representative value for the charge carrier density N_{CV}. Finally, cathodo-luminescence spectra were measured on CZTSSe/Mo/glass substrates under normal e-beam incidence in a FE-SEM (FEI Inspect F50), using an acceleration voltage of 20 kV and an e-beam current of 3.6 nA. The emitted light was collected via a half-parabolic mirror, a spectrometer Horiba iHR550 (0.5 mm entrance slit) with a 150 l/mm IR grating (centered at 1200 nm) and an InGaAs array detector (Andor Technology). Quantitative and comparable data are based on i) maximum signal achieved after adjustment of the geometrical settings at each measurement point, ii) signal averaged on a 10 × 10 µm sample area.

Acknowledgments

G.D., G.L and S.B. conceived and led the project, S.B. monitored the literature, G.L. supervised most of the experimental work, B.D., C.M., C.C and A.J. carried out the fabrication of the CZTSSe samples and devices. The I(V) and IQE data were collected by C.C., C.M. and G.L. The optical measurements to derive *Eg* and photoluminescence were performed by G.R and S.S. The C(V) measurements were performed by G.R. The STEM analysis was conducted by B.D. The XRD refinement analysis was conducted by A.L. The CL measurements were performed by F.D., S.B. and G.D wrote the manuscript, with contributions and feedback from all co-authors; In particular, S.S. wrote the review section 3.2.3, and A.W. reviewed the section 3.2.1. The work at Bath was supported by the EPSRC (Grant No. EP/K016288/1 and EP/L017792/1) and the ERC (Starting Grant 27757).

Received: November 16, 2015
Revised: January 29, 2016
Published online:

[1] D. B. Mitzi, O. Gunawan, T. K. Todorov, D. A. R. Barkhouse, *Phil. Trans. R. Soc. A* **2013**, *371*, 1996.
[2] W. Wang, M. T. Winkler, O. Gunawan, T. Gokmen, T. K. Todorov, Y. Zhu, D. B. Mitzi, *Adv. Energy Mater.* **2013**, *4*, 1301465.
[3] J. Kim, H. Hiroi, T. K. Todorov, O. Gunawan, M. Kuwahara, T. Gokmen, D. Nair, M. Hopstaken, B. Shin, Y. S. Lee, W. Wang, H. Sugimoto, D. B. Mitzi, *Adv. Mater.* **2014**, *26*, 7427.
[4] Best Research-Cell Efficiency chart, regularly updated by NREL, http://www.nrel.gov/ncpv/images/efficiency_chart.jpg (accessed: July 2015).
[5] A. Polizzotti, I. L. Repins, R. Noufi, S.-H. Wei, D. B. Mitzi, *Energy Environ. Sci.* **2013**, *6*, 3171.
[6] T. Gokmen, O. Gunawan, T. K. Todorov, D. B. Mitzi, *Appl. Phys. Lett.* **2013**, *103*, 103506.
[7] *Copper Zinc Tin Sulfide-Based Thin Film Solar Cells*, (Ed: K. Ito), Wiley, UK **2015**, pp. 55–73.
[8] J. J. Scragg, L. Choubrac, A. Lafond, T. Ericson, C. Platzer-Björkman, *Appl. Phys. Lett.* **2014**, *104*, 041911.
[9] G. Rey, A. Redinger, J. Sendler, T. P. Weiss, M. Thevenin, M. Guennou, B. E. Adib, S. Siebentritt, *App. Phys. Lett.* **2014**, *105*, 112106.
[10] C. Krammer, C. Huber, C. Zimmermann, M. Lang, T. Schnabel, T. Abzieher, E. Ahlswede, H. Kalt, M. Hetterich, *App. Phys. Lett.* **2014**, *105*, 262104.
[11] M. T. Winkler, W. Wang, O. Gunawan, H. J. Hovel, T. K. Todorov, D. B. Mitzi, *Energy Environ. Sci.* **2014**, *7*, 1029.
[12] K. Sardashti, R. Haight, T. Gokmen, W. Wang, L.-Y. Chang, D. B. Mitzi, A. C. Kummerl, *Adv. Energy Mater.* **2015**, *5*, 1402180.
[13] H. Xin, S. M. Vorpahl, A. D. Collord, I. L. Braly, A. R. Uhl, B. W. Krueger, D. S. Ginger, H. W. Hillhouse, *Phys. Chem. Chem. Phys.* **2015**, *17*, 23859.
[14] S. G. Haass, M. Diethelm, M. Werner, B. Bissig, Y. E. Romanyuk, A. N. Tiwari, *Adv. Energy Mater.* **2015**, DOI: 10.1002/aenm.201500712.
[15] G. Larramona, S. Levcenko, S. Bourdais, A. Jacob, C. Choné, B. Delatouche, C. Moisan, T. Unold, G. Dennler, *Adv. Energy Mater.* **2015**, *5*, 1501404.
[16] T. Schnabel, T. Abzieher, M. Friedlmeier, E. Ahlswede, *IEEE J. Photovolt.* **2015**, *5*, 670.
[17] C. J. Hages, S. Levcenco, C. K. Miskin, J. H. Alsmeier, D. Abou-Ras, R. G. Wilks, M. Bär, T. Unold, R. Agrawal, *Prog. Photovolt: Res. Appl.* **2015**, *23*, 376.
[18] Z. Su, J. M. R. Tan, X. Li, X. Zeng, S. K. Batabyal, L. H. Wong, *Adv. Energy Mater* **2015**, *5*, 1500682.
[19] W. Wu, Y. Cao, J. V. Caspar, Q. Guo, L. K. Johnson, I. Malajovich, H. D. Rosenfeld, K. R. Choudhury, *J. Mater Chem. C* **2014**, *2*, 3777.
[20] C. K. Miskin, W.-C. Yang, C. J. Hages, N. J. Carter, C. S. Joglekar, E. A. Stach, R. Agrawal, *Prog Photovolt: Res Appl.* **2015**, *23*, 654.
[21] H. Hiroi, N. Sakai, Y. Iwata, T. Kato, H. Sugimoto, *Proc. 42nd IEEE PVSC Conference*, USA **2015**.
[22] Y. S. Lee, T. Gershon, O. Gunawan, T. Todorov, T. Gokmen, Y. Virgus, S. Guha, *Adv. Energy Mater.* **2014**, *4*, 1401372.
[23] K. Furuta, N. Sakai, T. Kato, H. Sugimoto, Y. Kurokawa, A. Yamada, *Phys. Status Solidi C* **2015**, *12*, 704.
[24] S. Giraldo, M. Neuschitzer, T. Thersleff, S. Lopez-Marino, Y. Sanchez, X. Haibing, M. Placidi, P. Pistor, V. Izquierdo-Roca, K. Leifer, A. Pérez-Rodríguez, E. Saucedo, *Adv. Energy Mater.* **2015**, *5*, 1501070.
[25] S. G. Choi, T. J. Kim, S. Y. Hwang, J. Lia, C. Persson, Y. D. Kim, S.-H. Wei, I. L. Repins, *Sol. Energy Mat. Sol. Cells* **2014**, *130*, 375.
[26] G. Brammertz, M. Buffière, S. Oueslati, H. ElAnzeery, K. B. Messaoud, S. Sahayaraj, C. Köble, M. Meuris, J. Poortmans, *Appl. Phys. Lett.* **2013**, *103*, 163904.
[27] M. A. Green, K. Emery, Y. Hishikawa, W. Warta, E. D. Dunlop, *Solar Cell Efficiency Tables (version 46) Prog. Photovolt: Res. Appl.* **2015**, *23*, 805.
[28] H. Sugimoto, C. Liao, H. Hiroi, N. Sakai, T. Kato, *Proc. 39th IEEE Photovoltaic Specialists Conference (PVSC)* **2013**, *3208*.
[29] M. Boccard, C. Battaglia, S. Hänni, K. Söderström, J. Escarré, S. Nicolay, F. Meillaud, M. Despreisse, C. Ballif, *Nano Lett.* **2012**, *12*, 1344.
[30] H. ElAnzeery, O. El Daif, M. Buffière, S. Oueslati, K. Ben Messaoud, D. Agten, G. Brammertz, R. Guindi, B. Kniknie, M. Meuris, J. Poortmans, *Phys. Status Solidi A.* **2015**, *212*, 1984.
[31] K. Ben Messaoud, M. Buffière, G. Brammertz, H. ElAnzeery, S. Oueslati, J. Hamon, B. J. Kniknie, M. Meuris, M. Amlouk, J. Poortmans, *Prog. Photovolt: Res Appl.* **2015**, *23*, 1608.

© 2016 WILEY-VCH Verlag GmbH & Co. KGaA, Weinheim

[32] Y. Yan, *Proc. 37th IEEE Photovoltaic Specialists Conference (PVSC)* **2011**, 001218.
[33] I. Repins, C. Beall, N. Vora, C. DeHart, D. Kuciauskas, P. Dippo, B. To, J. Mann, W.-C. Hsu, A. Goodrich, R. Noufi, *Sol. Energy Mat. Sol. Cells* **2012**, *10*, 154.
[34] I. Malajovich, Y. Cao, J. V. Caspar, Q. Guo, L. K. Johnson, B. Ma, K. R. Choudhury, D. J. Walls, W. Wu, *Proc. 40th IEEE Photovoltaic Specialist Conference (PVSC)* **2014**, 2370.
[35] L. Grenet, D. Bernardi, D. Kohen, C. Lepoittevin, S. Noël, N. Karst, A. Brioude, S. Perraud, H. Mariette, *Sol. Energy Mat. Sol. Cells* **2012**, *101*, 11.
[36] M. Buffière, G. Brammertz, A.-A. El Mel, N. Lenaers, Y. Ren, A. E. Zaghi, Y. Mols, C. Koeble, J. Vleugels, M. Meuris, J. Poortmans, *Proc. 39th IEEE Photovoltaic Specialists Conference (PVSC)* **2013**, 1941.
[37] H. Hiroi, N. Sakai, T. Kato, H. Sugimoto, *Proc. 39th IEEE Photovoltaic Specialists Conference (PVSC)* **2013**, 0863.
[38] Q. Guo, G. M. Ford, W.-C. Yang, B. C. Walker, E. A. Stach, H. W. Hillhouse, R. Agrawal, *J. Am. Chem. Soc.* **2010**, *132*, 17384.
[39] Y. Cao, M. S. Denny, J. V. Caspar, W. E. Farneth, Q. Guo, A. S. Ionkin, L. K. Johnson, M. Lu, I. Malajovich, D. Radu, H. D. Rosenfeld, K. R. Choudhury, W. Wu, *J. Am. Chem. Soc.* **2012**, *134*, 15644.
[40] W. Ki, H. W. Hillhouse, *Adv. Energy Mater.* **2011**, *1*, 732.
[41] D. Mutter, S. T. Dunham, *Proc. 40th IEEE Photovoltaic Specialists Conference (PVSC)* **2014**, 2390.
[42] a) G. Larramona, S. Bourdais, A. Jacob, C. Choné, T. Muto, Y. Cuccaro, B. Delatouche, C. Moisan, D. Péré, G. Dennler, *RSC Adv.* **2014**, *4*, 14655; b) S. Bourdais, C. Choné, Y. Cuccaro, WO 2014/016489 A2 (France).
[43] a) G. Larramona, S. Bourdais, A. Jacob, C. Choné, T. Muto, Y. Cuccaro, B. Delatouche, C. Moisan, D. Péré, G. Dennler, *J. Phys. Chem. Lett.* **2014**, *5*, 3763; b) A. Jacob, C. Choné, G. Larramona, B. Delatouche, S. Bourdais, G. Dennler, WO 2015/185834 A1 (France).
[44] D. Colombara, A. Crossay, L. Vauche, S. Jaime, M. Arasimowicz, P.-P. Grand, J. P. Dale, *Phys. Status Solidi A.* **2015**, *212*, 88.
[45] L. M. Peter, *Electrochem. Comm.* **2015**, *50*, 88.
[46] F. Jiang, S. Ikeda, T. Harada, M. Matsumura, *Adv. Energy Mater.* **2013**, *4*, 1301381.
[47] T. Gershon, B. Shin, N. Bojarczuk, M. Hopstaken, D. B. Mitzi, S. Guha, *Adv. Energy Mater.* **2015**, *5*, 1400849.
[48] J. V. Li, D. Kuciauskas, M. R. Young, I. L Repins, *Appl. Phys. Lett.* **2013**, *10*, 163905.
[49] A. Nagaoka, H. Miyake, T. Taniyama, K. Kakimoto, Y. Nose, M. A. Scarpulla, *Appl. Phys. Lett.* **2014**, *104*, 152101.
[50] H. Guo, Y. Cui, A. Tian, S. Gao, G. Wang, D. Pan, *Cryst. Growth Des.* **2015**, *15*, 771.
[51] A. Carrete, A. Shavel, X. Fontané, J. Montserrat, J. Fan, M. Ibáñez, E. Saucedo, A. Pérez-Rodriguez, A. Cabot, *J. Am. Chem. Soc.* **2013**, *135*, 15982.
[52] D.-H. Kuo, M. Tsega, *Mat. Res. Bull.* **2014**, *49*, 608.
[53] a) G. M. Ford, Q. Guo, R. Agrawal, H. W. Hillhouse, *Chem. Mater.* **2011**, *23*, 2626; b) D. B. Khadka, J. Kim, *J. Phys. Chem. C* **2015**, *119*, 1706.
[54] C. J. Hages, M. J. Koeper, R. Agrawal, *Sol. Energy Mat. Sol. Cells.* **2016**, *145*, 342.
[55] P. Jackson, D. Hariskos, R. Wuerz, O. Kiowski, A. Bauer, T. M. Friedlmeier, M. Powalla, *Phys. Stat. Sol. (RRL)* **2015**, *9*, 28.
[56] M. A. Contreras, J. Tuttle, D. Du, Y. Qi, A. Swartzlander, A. Tennant, R. Noufi, *App. Phys. Lett.* **1993**, *63*, 1824.
[57] T. Kato, N. Sakai, H. Sugimoto, *Proc. 40th IEEE Photovoltaic Specialist Conference (PVSC)* **2014**, 844.
[58] M. A. Contreras, J. Tuttle, A. Gabor, A. Tennant, K. Ramanathan, S. Asher, A. Franz, J. Keane, L. Wang, J. Scofield, R. Noufi, *Proc. 24th IEEE Photovoltaic Specialists Conference (PVSC)* **1994**, *1*, 68.
[59] I. Kim, K. Kim, Y. Oh, K. Woo, G. Cao, S. Jeong, J. Moon, *Chem. Mater.* **2014**, *26*, 3957.
[60] T. K. Todorov, J. Tang, S. Bag, O. Gunawan, T. Gokmen, Y. Zhu, D. B. Mitzi, *Adv. Energy Mater.* **2013**, *3*, 34.
[61] U. Rau, J. H. Werner, *Appl. Phys. Lett.* **2004**, *84*, 3735.
[62] H. Xie, M. Dimitrievska, X. Fontané, Y. Sánchez, S. López-Marino, V. Izquierdo-Roca, V. Bermudez, A. Pérez-Rodriguez, E. Saucedo, *Sol. Energy Mat. Sol. Cells* **2015**, *40*, 289.
[63] M. M. Islam, M. A. Halim, T. Sakurai, N. Sakai, T. Kato, H. Sugimoto, H. Tampo, H. Shibata, S. Niki, K. Akimoto, *Appl. Phys. Lett.* **2015**, *106*, 243905.
[64] K. F. Tai, T. Gershon, O. Gunawan, C. H. A. Huan, *J. Appl. Phys.* **2015**, *117*, 235701.
[65] M. Courel, J. A. Andrade-Arvizu, O. Vigil-Galan, *Solid-State Electronics* **2015**, *111*, 243.
[66] K. Wang, O. Gunawan, T. Todorov, B. Shin, S. J. Chey, N. A. Bojarczuk, D. B. Mitzi, S. Guha, *Appl. Phys. Lett.* **2010**, *97*, 143508.
[67] a) S. Chen, X. G. Gong, A. Walsh, S.-H. Wei, *App. Phys. Lett.* **2010**, *96*, 021902; b) S. Chen, A. Walsh, X.-G. Gong, S.-H. Wei, *Adv. Mater.* **2013**, *25*, 1522.
[68] D. Han, Y. Y. Sun, J. Bang, Y. Y. Zhang, H.-B. Sun, X.-B Li, S.-B. Zhang, *Phys. Rev. B.* **2013**, *87*, 155206.
[69] K. P. Choudhury, Y. Cao, J. V. Caspar, W. E. Farneth, Q. Guo, A. S. Ionkin, *Proc. 38th IEEE Photovoltaic Specialists Conference (PVSC)* **2012**, 001471.
[70] A. D. Collord, H. Xin, H. W. Hillhouse, *IEEE J. Photovolt.* **2014**, *5*, 288.
[71] A. Lafond, L. Choubrac, C. Guillot-Deudon, P. Deniard, S. Jobic, *Z. Anorg. Allg. Chem.* **2012**, *638*, 2517.
[72] G. Gurieva, M. Dimitrievska, S. Zander, A. Pérez-Rodríguez, V. Izquierdo-Roca, S. Schorr, *Phys. Stat. Sol. C* **2015**, *12*, 588.
[73] J. Mattheis, U. Rau, J. Werner, *J. Appl. Phys.* **2007**, *101*, 113519.
[74] A. Fairbrother, M. Dimitrievska, Y. Sánchez, V. Izquierdo-Roca, A. Pérez-Rodríguez, E. Saucedo, *J. Mater. Chem. A.* **2015**, *3*, 9451.
[75] D. W. Miller, C. W. Warren, O. Gunawan, T. Gokmen, D. B. Mitzi, J. D. Cohen, *Appl. Phys. Lett.* **2012**, *101*, 142106.
[76] S. De Wolf, J. Holovsky, S.-J. Moon, P. Löper, B. Niesen, M. Ledinsky, C. Ballif, *J. Phys. Chem. Lett.* **2014**, *5*, 1035.
[77] S. Siebentritt, G. Rey, A. Finger, J. Sendler, T. P. Weiss, D. Regesch, T. Bertram, *Sol. Energy Mat. Sol. Cells* **2015**, DOI: 10.1016/j.solmat.2015.10.017.
[78] T. Gokmen, O. Gunawan, D. B. Mitzi, *Appl. Phys. Lett.* **2014**, *105*, 033903.
[79] a) V. Dobrego, I. Shlimak, *Phys. Stat. Sol. B.* **1969**, *33*, 805; b) Z. I. Alferov, V. M. Andreev, D. Z. Garbuzov, M. K. Trukan, *Soviet Physics – Semicond.* **1973**, *6*, 1718; c) P. W. Yu, *J. Appl. Phys.* **1977**, *48*, 5043.
[80] a) H. P. Gislason, B. H. Yang, J. Pétursson, M. K. Linnarsson, *J. Appl. Phys.* **1993**, *74*, 7275; b) I. Dirnstorfer, M. Wagner, D. M. Hofmann, M. D. Lampert, F. Karg, B. K. Meyer, *Phys. Stat. Sol. A.* **1998**, *168*, 163; c) J. Larsen, K. Burger, L. Gütay, S. Siebentritt, *Proc. 37th IEEE Photovoltaic Specialist Conference*, Seattle **2011**, *396*.
[81] Y. S. Yee, B. Magyari-Köpe, Y. Nishi, S. F. Bent, B. M. Clemens, *Phys. Rev. B.* **2015**, *92*, 195201.
[82] S. Schorr, *Sol. Energy Mat. Sol. Cells* **2011**, *95*, 1482.
[83] A. Lafond, L. Choubrac, C. Guillot-Deudon, P. Fertey, M. Evain, S. Jobic, *Acta Crystallogr. B Struct. Sci. Cryst. Eng. Mater.* **2014**, *70*, 390.
[84] S. Schorr, H. J. Hoebler, M. Tovar, *Eur. J. Mineral.* **2007**, *19*, 65.
[85] G. H. Vineyard, *Phys. Rev.* **1956**, *102*, 981.

© 2016 WILEY-VCH Verlag GmbH & Co. KGaA, Weinheim

[86] L. Choubrac, M. Paris, A. Lafond, C. Guillot-Deudon, X. Rocquefelte, S. Jobic, *Phys. Chem. Chem. Phys.* **2013**, *15*, 10722.
[87] M. Grossberg, J. Krustok, T. Raadik, M. Kauk-Kuusik, J. Raudoja, *Curr. Appl. Phys.* **2014**, *14*, 1424.
[88] A. Redinger, J. Sendler, R. Djemour, T. P. Weiss, G. Rey, P. J. Dale, S. Siebentritt, *IEEE J. Photovolt.* **2014**, *5*, 641.
[89] J. J. S. Scragg, J. K. Larsen, M. Kumar, C. Persson, J. Sendler, S. Siebentritt, C. Platzer Björkman, *Phys. Stat. Sol. B.* **2016**, *253*, 247.
[90] M. Paris, L. Choubrac, A. Lafond, C. Guillot-Deudon, S. Jobic, *Inorg. Chem.* **2014**, *53*, 8646.
[91] M. Y. Valakh, O. F. Kolomys, S. S. Ponomaryov, V. O. Yukhymchuk, I. S. Babichuk, V. Izquierdo-Roca, E. Saucedo, A. Pérez-Rodriguez, J. R. Morante, S. Schorr, I. V. Bodnar, *Phys. Stat. Sol. (RRL)* **2013**, *7*, 258.
[92] C. Krammer, C. Huber, T. Schnabel, C. Zimmermann, M. Lang, E. Ahlswede, H. Kalt, M Hetterich, *Proc. 42nd IEEE Photovoltaic Specialist Conference (PVSC)* **2015**, DOI: 10.1109/PVSC.2015.7356096.
[93] S. Chen, X. G. Gong, A. Walsh, S.-H. Wei, *Appl. Phys. Lett.* **2009**, *94*, 041903.
[94] D. Huang, C. Persson, *Thin Solid Films* **2013**, *535*, 265.
[95] S. Chen, A. Walsh, J. Yang, X.-G. Gong, L. Sun, P. Yang, J. Chu, S.-H. Wei, *Phys. Rev. B* **2011**, *83*, 125201.
[96] P. Zawadzki, A. Zakutayev, S. Lany, *Phys. Rev. Appl.* **2015**, *3*, 34007.
[97] G. Rey, T. P. Weiss, J. Sendler, A. Finger, F. Werner, M. Melchiore, S. Siebentritt, submitted to *Sol. Energy Mat. Sol. Cells*.
[98] a) W. Ki, H. W. Hillhouse, *Adv. Energy Mater.* **2011**, *1*, 732; b) S. Levcenco, D. Dumcenco, Y. P. Wang, Y. S. Huang, C. H. Ho, E. Arushanov, V. Tezlevan, K. K. Tiong, *Opt. Mater.* **2012**, *34*, 1362.
[99] K. E. Roelofs, Q. Guo, S. Subramoney, J. V. Caspar, *J. Mater. Chem. A.* **2014**, *2*, 13464.
[100] *The Rietveld Method* (Ed: R. A. Young), Oxford University Press and the International Union of Crystallography, UK **2000**, 259.2.
[101] M. Paris, G. Larramona, P. Bais, S. Bourdais, A. Lafond, C. Choné, C. Guillot-Deudon, B. Delatouche, C. Moisan, G. Dennler, *J. Phys. Chem. C* **2015**, *119*, 26849.
[102] W. Shockley, H. J. Queisser, *J. Appl. Phys.* **1961**, *32*, 510.
[103] R. Djemour, A. Redinger, M. Mousel, L. Gutay, S. Siebentritt, *J. App. Phys.* **2014**, *116*, 073509.
[104] W.-J. Yin, Y. Wu, S.-H Wei, R. Noufi, M. M. Al-Jassim, Y. Yan, *Adv. Energy Mater.* **2014**, *4*, 1300712.
[105] J. K. Larsen, S.-Y. Li, J. J. Scragg, Y. Ren, C. Hägglund, M. D. Heinemann, S. Kretzschmar, T. Unold, C. Platzer-Björkman, *J. Appl. Phys.* **2015**, *118*, 035307.
[106] M. Neuschitzer, Y. Sanchez, T. Olar, T. Thersleff, S. Lopez-Marino, F. Oliva, M. Espindola-Rodriguez, H. Xie, M. Placidi, V. Izquierdo-Roca, I. Lauermann, K. Leifer, A. Pérez-Rodriguez, E. Saucedo, *Chem Mater.* **2015**, *27*, 5279.
[107] R. C. Alig, S. Bloom, *Phys. Rev. Lett.* **1975**, *35*, 1522.
[108] P. Xu, S. Chen, B. Huang, H. J. Xiang, X.-G Gong, S.-H. Wei, *Phys Rev B.* **2013**, *88*, 045427.
[109] Y. Yan, W.-J. Yin, T. Shi, F. Hong, J. Ge, Y. Yue, W. Ke, D. Zhao, A. Cimaroli, In: *22nd International Workshop on Active-Matrix Flatpanel Displays and Devices (AM-FPD)* **2015**, *57*.
[110] W. E. Vargas, D.E. Azofeifa, N. Clark, *Thin Solid Films* **2003**, *425*, 1.
[111] J. H. Scofield, *Sol. Energy Mater. Sol. Cells* **1995**, *37*, 217.
[112] G. L. Miller, *IEEE Trans. Electron. Devices* **1972**, *19*, 1103.

© 2016 WILEY-VCH Verlag GmbH & Co. KGaA, Weinheim